https://doi.org/10.5194/egusphere-2026-3978
Preprint. Discussion started: 24 September 2026

Gravity disturbance maps and updated gravity anomaly maps in French-Belgian Hainaut from recent gravity acquisitions and legacy data

Quentin CAMPEOL[1], Nicolas DUPONT[1] and Olivier KAUFMANN[1]

[1]Department of Geology and Applied Geology, University of Mons, Faculty of Engineering, 9, rue de Houdain, 7000 Mons, Belgium

Correspondence to: Quentin CAMPEOL (quentin.campeol@umons.ac.be)

Keywords: Refined Bouguer anomaly; Topography-free gravity disturbance; Absolute gravity referencing; Gravity acquisition; Topographic correction; Equivalent-sources gridding.

Abstract

In Wallonia, the centre of Hainaut (SW Belgium) is considered the main area where deep geothermal resources are proven. In this region bordering France, the productive geothermal resource is located within karstified levels resulting from the dissolution of interbedded massive anhydrites in the Carboniferous limestones. To improve current knowledge of deep geological structures and to better delineate the geothermal targets, new detailed regional gravity anomaly and disturbance maps have been produced. These include maps of the observed gravity, free-air anomaly, refined Bouguer anomaly, gravity disturbance, topography-free gravity disturbance.

This has involved the compilation and harmonisation of cross-border legacy and recent gravity data, combined with an homogeneous reprocessing and an interpolation using the equivalent source method. The legacy data come from the Belgian and French databases published by the ROB (Belgium) and BRGM (France) respectively, to which unpublished data from the Battaille 1967 campaign have been added after their retro-processing from Bouguer anomaly data. The new gravity data come from the recent MoreGeo 2019-2022 gravity acquisition campaign. This campaign covers an area of 820 km² with 3,784 gravity stations distributed along densely sampled lines and displays a RMSE range of 41.9 to 67.5 µgal after absolute gravity referencing. The gravimetric processing works presented in this paper rely on open-source Python libraries. These include an advanced total correction budget evaluation and topographic correction up to 167 km² in extent. The resulting maps are consistent with previous ones, in particular the strong correlation between the anomaly and the thickness of the Meso-Cenozoic deposits. It also shows new anomalies that may be due to deep-seated structures. It will be used as a basis for modelling the geothermal reservoir, provided that the effect of the Meso-Cenozoic deposits is accounted for.

1 Introduction

1.1 Geological and geophysical context

In Belgium, numerous gravity surveys have been carried out for more than a century. The various acquisition campaigns related in Verbeurgt et al. (2019) have made it possible to increase the density of the network of gravimetric stations throughout the country and to refine the mapping of the Bouguer anomaly in Belgium (Everaerts and De Vos, 2012). The most recent mapping from this latter work is notably shown in Fig. A1 in Appendix. The gravity data used to produce this map are currently available in public databases. These are the gravity database published by the Royal Observatory of Belgium (ROB) for the Belgian data (Verbeurgt et al., 2019) and the "Banque Gravimétrique de France" for the French data (BRGM, 2023). The main shortcoming of these Bouguer anomaly maps in the Mons region is the spatial density of the gravity stations which is sparse and unevenly distributed, particularly in the south of this zone along the French border.

The Mons area, considered to be the main area where deep geothermal resources are known in Wallonia (Petitclerc and Vanbrabant, 2011), would benefit from in-depth knowledge of gravity anomalies (Kaufmann et al., 2025). On the simplified geological map (Fig. 1a) and the structural map (Fig. 1b), the carboniferous limestones of the Brabant Parautochton tectonic unit occur in the northern part along a mainly West-East axis. They plunge southwards below thrust sheets (cf. Fig. 1c): (1)

https://doi.org/10.5194/egusphere-2026-3978
Preprint. Discussion started: 24 September 2026

the Haine-Sambre-Meuse overturned thrust sheets, mainly composed by Upper Carboniferous coal measures and (2) the Ardennes Allochton, made by folded Devonian formations, mainly sandstones and shales in this area. The base of the Ardennes allochton is a main thrust fault called «Midi(-Eifel) Fault» in France and Belgium. These tectonic units are covered by younger Meso-Cenozoic formations in the center of the area (Belanger et al., 2012; Mansy et al., 1999).

Massive anhydrite layers at depth are interbedded in the Carboniferous limestones as revealed by the Saint-Ghislain borehole. Their average density is 3.5 (Campeol, 2021), much higher than that of their limestone host. These evaporitic levels, which appear on the surface as dissolution breccias, show significant karstification at depth and therefore represent the most permeable and productive part of the geothermal reservoir (Kaufmann et al., 2025). In the region, three geothermal plants exploit the productive zones of this karstic reservoir, located at depths of between 1,350 and 2,500 m depending on their location. The limited knowledge and the karstic nature of this reservoir mean that there are major uncertainties regarding the implementation of new geothermal projects. This is why, since the 2010s, a series of geophysical campaigns including seismic reflection (Dupont, 2021), have been carried out to constrain the geometry of the geothermal reservoir.

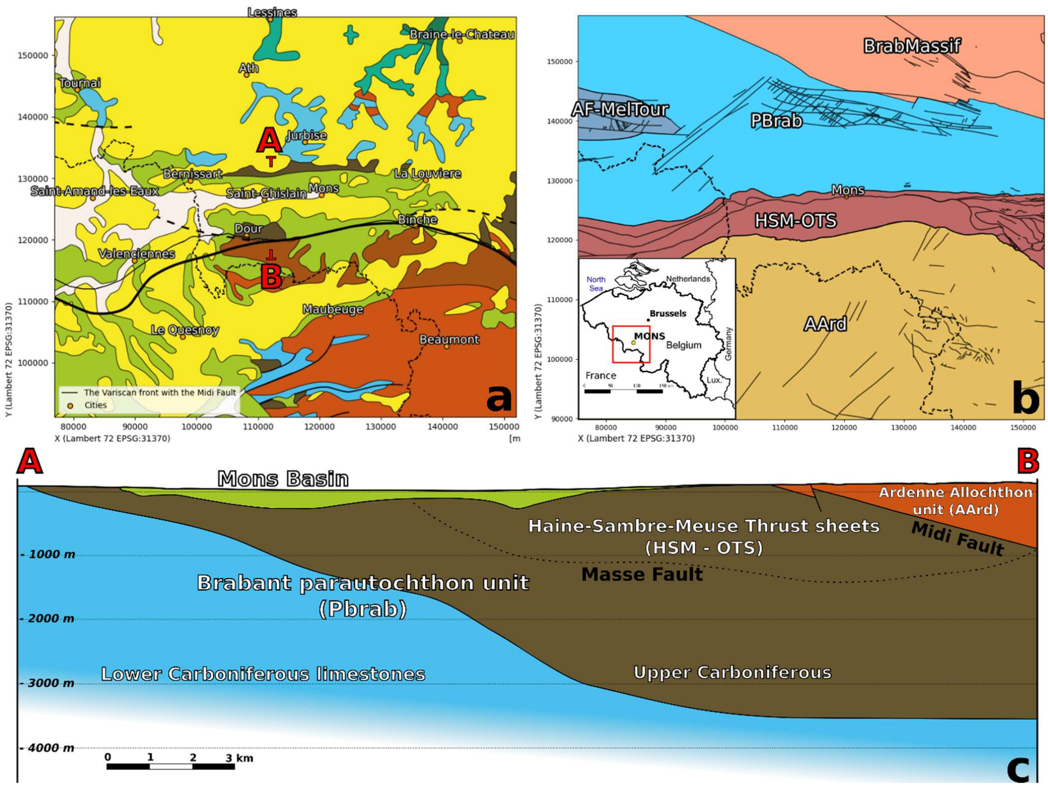

Figure 1: Simplified geological (a) and structural (b) maps of the study area (S-W Belgium). Mbasin : the Mons Basin, Pbrab : the Brabant Parautochthon, HSM-OTS : the Haine-Sambre-Meuse Overturned Thrust sheets, Aard : the Ardenne Allochthon, BrabMassif : the Brabant Massif and the AF-MelTour : the Melantois-Tournaisis faulted anticlinal. Predictive geological section (c) along the A-B direction (North-South), modified from (Dupont, 2021).

2D gravimetric modelling was carried out by Dr. Michel Everaerts and reported in (Dupont et al., 2023) on north-south sections. The modeling was guided by geological structures derived from seismic interpretations and a density model assigned to the various units. This direct modeling failed to reproduce the Bouguer anomaly of (Everaerts and De Vos, 2012) and resulted in unrealistic models of the subsurface density distribution. This highlighted the need to revise the anomaly maps in the area (and to redesign the regional deep geological model). In addition, improving the mapping of the anomaly in this regional geological context would allow for a more accurate characterization of any future modeling of the

https://doi.org/10.5194/egusphere-2026-3978
Preprint. Discussion started: 24 September 2026

geothermal reservoir Laurent (2021). Indeed, its brecciated zones and massive anhydrite zones could appear as negative and positive anomalies respectively, provided that the influence of the Meso-Cenozoic deposits is accounted for (Campeol et al., 2024b). Because of all this, the MoreGeo 2019-2022 gravity acquisition campaign was planned in 2019.

Dupont (2021) compiled archival documents including the Battaille 1967 dataset, an unpublished dataset which was not included in the ROB database. However, only the Bouguer anomaly values calculated with a reduction density of 2.1 g cm^{-3} were found in the archives of the Belgian Geological Survey. It has therefore not yet been mapped in conjunction with the data used by (Everaerts and De Vos, 2012), mainly because of the different reduction densities used in the corrections. Refining the regional Bouguer anomaly map needs thus to gather all gravity data available in the area by standardising the corrections applied to the various data sources.

In Belgium, it should also be noted that, only the Bouguer anomaly has been mapped without considering topographic effects. The other gravity anomaly fields (free-air anomaly, refined Bouguer anomaly, gravity disturbance and topography-free gravity disturbance) have never been the subject of an in-depth study, neither regional nor national mapping. It was therefore proposed to process these various maps since, in addition to its novelty, the gravity disturbance would be particularly preferable to the Bouguer anomaly for a geophysical study such as this one (Oliveira jr et al., 2018). The Sect. 2 presents hereafter the compilation and the fusion of the new datasets of MoreGeo 2019-2022 with all the regional legacy gravity data. Sect. 3 is devoted to the calculation and mapping of gravity anomalies and disturbances. All the work carried out was implemented using Python 3 notebooks and modules based on open-source tools written by authors exclusively.

1.2 Concepts of physical geodesy used

Gravity anomaly fields provide information about the distribution of geological masses in the subsurface. According to Eq. (2-224) of Hofmann-Wellenhof and Moritz (2006), they are defined on the basis of the anomalous potential T. It represents the comparison between the actual gravity potential $W_{(x, y, z)}$ and the normal gravity potential $U_{(x, y, z)}$, a theoretical gravity potential predicted by a normal gravity model, such as:

$$\boldsymbol{T(x,y,z) = W(x,y,z) - U(x,y,z)} \tag{1}$$

If we define the geoid as an equipotential surface from the specific actual gravity potential $W_{(x, y, z)} = W_0$ and the ellipsoid, an equipotential surface from the normal gravity potential such that $U_{(x, y, z)} = W_0$, we can define four specific geometric points and three specific heights. P is the position of a station on the earth surface and P_0 is the cross-point between the plumb line through P and the geoid ($|P\,P_0|=H$). In this work, the geoid is replaced by the concept of a quasi-geoid (Molodensky et al., 1960); P_0 is then defined as the cross-point between the ellipsoidal normal through P and the quasigeoid ($|P\,P_0|=H^*$). Q_0 is the common (cross-)point of the ellipsoidal normal through P and the ellipsoid ($|P\,Q_0|=h$) and Q is the point on the ellipsoidal normal through P at the same height above the ellipsoid as P is above the (quasi)geoid. In terms of the gravitational vector, according to Eq. (2-228) and (8-127) of Hofmann-Wellenhof and Moritz (2006) and using the Free-air (**F**) approximation, gravity anomaly and disturbance are determined as follows:

The free-air gravity anomaly:

$$\boldsymbol{grad}(\boldsymbol{W}(x_P, y_P, z_P)) - \boldsymbol{grad}(\boldsymbol{U}(x_Q, y_Q, z_Q)) = \mathbf{g}_P - \boldsymbol{\gamma}_Q = \mathbf{g}_P + \boldsymbol{F} - \boldsymbol{\gamma}_{Q_0} \approx \mathbf{g}_{P_0} - \boldsymbol{\gamma}_{Q_0} \equiv \boldsymbol{\Delta}\mathbf{g} \tag{2}$$

The gravity disturbance:

$$\boldsymbol{grad}(\boldsymbol{W}(x_P, y_P, z_P)) - \boldsymbol{grad}(\boldsymbol{U}(x_P, y_P, z_P)) = \mathbf{g}_P - \boldsymbol{\gamma}_P \equiv \boldsymbol{\delta}\mathbf{g} \tag{3}$$

The free-air reduction **F** enables to estimate $\mathbf{g}_{P_0}$ in the Eq. 2, the gravity reduced to a common reference gravity level (i.e. (quasi)geoid) ignoring any excess or deficit of mass above the reference level. Based on the evaluation of the current gravity vertical gradient ($\partial g/\partial H$), Hofmann-Wellenhof and Moritz (2006) used the normal gravity ($\boldsymbol{\gamma}$) to define the Free-air reduction, as a function of ellipsoidal height and approximate it as Taylor series in powers of h truncated at degree 2:

$$\mathbf{F} = -\frac{\partial g}{\partial H}\mathbf{H} \approx -\frac{\partial \gamma}{\partial h}\mathbf{H} = +\mathbf{0.3086H} \tag{4}$$

Where H represents the orthometric or normal height of the gravity station above the (quasi)geoid and h, the ellipsoidal height. When the height of the geoid varies rapidly over the scale of a gravity survey, as is the case in mountainous regions, this causes multimetric differences between H (or H*) and h and generates indirect effects (Talwani, 1998) that can affect the calculation of free-air and Bouguer reductions. In the case of the French Belgian gravity data, this effect is negligible

https://doi.org/10.5194/egusphere-2026-3978
Preprint. Discussion started: 24 September 2026

considering the topography encountered and the small variation in the height of the geoid compared to that of the ellipsoid.

Calculating the Eq. 2 requires also defining $\boldsymbol{\gamma_{Q_0}}$, the normal gravity at Q_0, expressed by the following Somigliana formula (Hofmann-Wellenhof and Moritz, 2006; Moritz, 1980):

$$\boldsymbol{\gamma = \gamma_{Q_0} = g_e \cdot \frac{1 + k\sin^2(\varphi)}{\sqrt{1 - e^2\sin^2(\varphi)}}} \quad (5)$$

Where φ is the latitude of the station and g_e, e^2 and k are respectively the normal gravity at the equator, the first eccentricity squared and a constant based on the normal gravity at the equator and poles and the equatorial and polar semi-axes. This Eq. 5 models centrifugal and gravity effects on the ellipsoid surface and is therefore based solely on station latitude and ellipsoidal parameters. In this study, the normal gravity used is derived from the WGS84 normal gravity model or from the International Ellipsoid of Hayford model, depending on the data used. $\boldsymbol{\gamma_Q}$ and $\boldsymbol{\gamma_P}$ are determined by evaluating the closed-form formula of the normal gravity, implemented in Boule python library (Fatiando a Terra Project et al., 2026). For analytical expression, refer to Lakshmanan (1991) or Li and Götze (2001) and Eq. 2-113 in Hofmann-Wellenhof & Moritz (2006). This closed-form formula avoids the need to use Eq. 5 (which is accurate only on the ellipsoid) in conjunction with a free-air reduction, which should be particularly useful in geophysics (Fatiando a Terra Project et al., 2026).

To consider the atmospheric mass variations above the measuring stations, an atmospheric correction ($\boldsymbol{\delta g_{Atm}}$) has also been applied to the $\boldsymbol{\Delta g}$ and the $\boldsymbol{\delta g}$ evaluation using Ecker and Mittermayer (1969) equation. This ensures consistency with $\boldsymbol{\gamma}$, calculated for an ellipsoid surrounded by a standard atmosphere whose mass is included in the normal potential:

$$\boldsymbol{\delta g_{Atm} = 0.874 - 9.9 * 10^{-5}H + 3.56 * 10^{-9}H^2} \ \ [\mathbf{mgal}] \quad (6)$$

As explained by Bullard (1936) and summarised by Nowell (1999), differences in elevation between the gravity observations and the surrounding topography influence the gravitational attraction. These two effects have a significant impact on the free-air anomaly and the gravity disturbance. The Simple Bouguer reduction ($\mathbf{A_B}$) eliminates the influence of masses located between the station's elevation and the reference elevation. In Eq. 6 and 7, the letter H denotes either H* or h, depending on whether it is used in the calculation of the $\boldsymbol{\Delta g}$ or $\boldsymbol{\delta g}$ respectively.

$$\mathbf{A_B = 2\pi G\rho H} \quad (7)$$

The terrain correction ($\mathbf{A_t}$) removes the effects of the topography to account for the mass deficits and surpluses associated with the relief around gravity stations. Introduced by (Hayford and Bowie, 1912), and popularised by (Hammer, 1939), recent methods are usually based on the digital modelling of topography using simple geometric shapes, such as prisms, tesseroids and mass lines (Heiskanen and Moritz, 1967; Heck and Seitz, 2007; Makhloof, 2008). The prisms method is based on (Nagy, 1966a), who introduce the calculation of the influence of rectangular prisms on the vertical component of the gravitational field at an observation point. This method, which is easy to implement numerically (Nagy, 1966b), has also been summarised by simplifying the expressions for the gravitational potential of a rectangular prism and its derivatives in (Nagy et al., 2000; Nagy et al., 2002). It is also possible to calculate the total effect of the topographic masses in a single step, known as topographic correction ($\mathbf{A_T}$):

$$\boldsymbol{A_T = A_B - A_t} \quad (8)$$

Applying these reductions and corrections to the gravity anomalies and disturbances defined above yields to:

The refined Bouguer anomaly:

$$\boldsymbol{\Delta g_B \equiv \Delta g - A_T} \quad (9)$$

The topography-free gravity disturbance:

$$\boldsymbol{\delta g_B \equiv \delta g - A_T} \quad (10)$$

2 Compilation and fusion of recent gravity acquisitions and legacy databases

Mapping the updated regional gravity anomaly and disturbance fields, involved collecting and fusing all available gravity datasets in the region. In this sense, three legacy gravity databases containing relevant French and Belgian old gravity datasets acquired since the mid-20th century have been brought together. These include the Belgian gravity database published by the Royal Observatory of Belgium (ROB) (Verbeurgt et al., 2019), the French gravity database (BRGM, 2023)

https://doi.org/10.5194/egusphere-2026-3978
Preprint. Discussion started: 24 September 2026

and data from the Battaille 1967 campaign carried out by CGG for Battaille Frères society (Battaille, 1967). To complete the dataset and resample the gravity anomalies and disturbances as explained in Sect 1.1, the MoreGeo 2019-2022 gravity acquisition campaign was started in 2019. The map shown in Fig. 2 represents these different datasets within a 20 km radius of the MoreGeo campaign data. This area represents the study zone in this work.

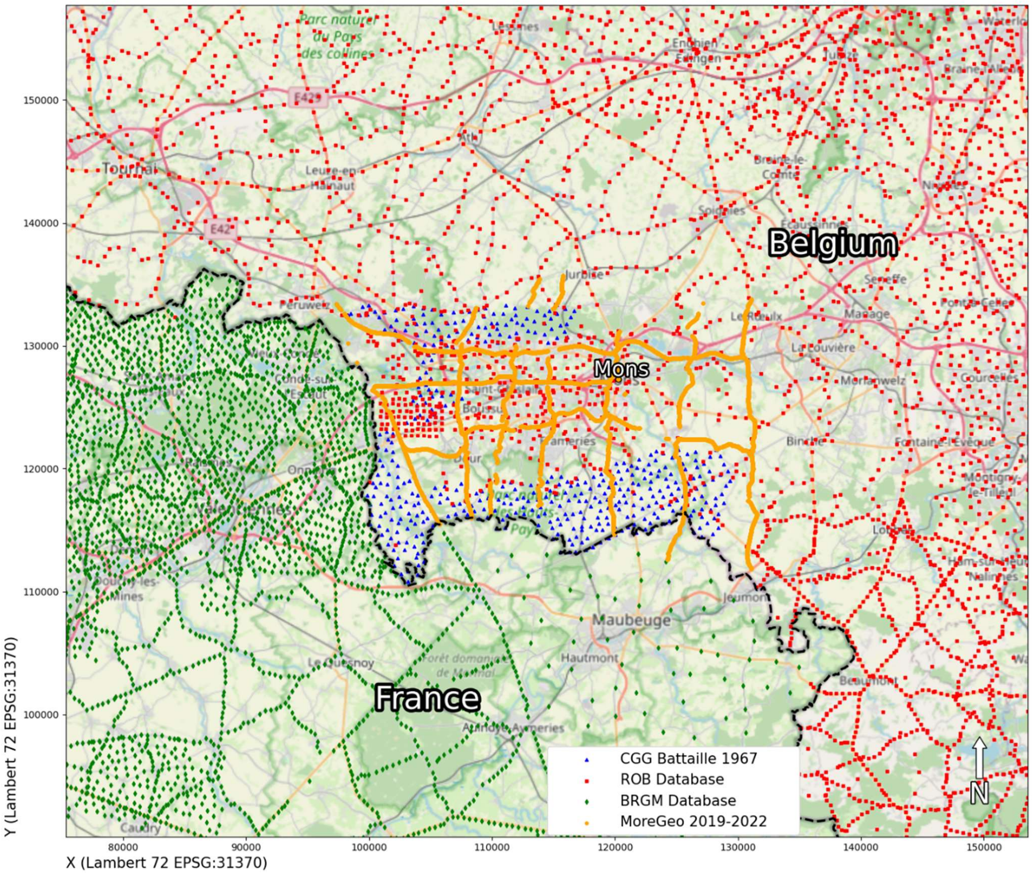

Figure 2: The different sources of gravity datasets brought together in this work. In red: the Belgian gravimetric database, published by the Royal Observatory of Belgium, from (Verbeurgt et al., 2019). In green: the French gravimetric database from (BRGM, 2023). In blue: The gravimetric campaign carried out for Battaille Frères society in 1967, from (Battaille, 1967). In orange: The MoreGeo2019-2022 gravity acquisition campaign. ©OpenStreetMap Distributed under the Open Data Commons Open Database License (ODbL) v1.0.

There are numerous challenges involved in merging these datasets. Some of these are absolute gravity databases (BRGM and ROB), whilst others consist of historical Bouguer anomaly data (Battaille 1967) and require retro-processing. The recent MoreGeo campaign required a precise evaluation of the total correction budget and an absolute gravity referencing. Another challenge is related to the geographical and altimetric reference systems to which the data sources are referenced.

2.1 Gravity databases of Belgium and France

The BRGM and ROB databases are absolute gravity databases; they therefore incorporate instrumental and temporal corrections into their gravimetric data. The French gravity database was published by BRGM (2023) and is regularly updated with data from new ground and airborne campaigns (Martelet and Deparis, 2010). The Belgian gravity database

https://doi.org/10.5194/egusphere-2026-3978
Preprint. Discussion started: 24 September 2026

was published by the Royal Observatory of Belgium. Verbeurgt et al. (2019) presented the work carried out in preparation for its publication, which involved the collection and standardisation of absolute gravimetric data obtained over the Belgian territory during numerous campaigns (±69,000 stations). In the study area, the following campaigns were selected: *2nd Belgian gravimetric network* (1948), *Mons* (1960), *Dinant basin* (1962), *extension 1948* (1972), *Geraardsbergen* (1993), *Central Belgium* (1996) and *Philippeville* (2000). It was necessary to reposition the stations belonging to the *Mons* (1960) and *Extension 1948* (1972) campaigns located in the center of the study area because of very significant positioning inaccuracies (Verbeurgt and Kazmierczak, Geodesy Service at the National Geographic Institute of Belgium, personal communication). Their associated metadata in the database indicates an implausible latitude and longitude accuracy of 0.45 decimal degrees. The origin of this problem could be related to truncated station location coordinates or incorrect georeferencing of an old map, but these hypotheses could not be confirmed. To incorporate these datasets, which cover important central and poorly sampled areas, it was decided to start over using their original documents from (Leclerc, 1960) and (Battaille, 1969). The original maps were meticulously georeferenced, and the stations were repositioned one by one based on the paths and roads indicated on these documents. This new positioning of the gravimetric stations results in positioning differences of up to 150 m. It should be noted that the vertical accuracy of these campaigns is 5 cm.

2.2 The new MoreGeo 2019-2022 acquisition campaign

2.2.1 Equipment used

The gravimetric campaign was carried out using a field micro-gravimeter, the Scintrex CG-6 Autograv™. According to the manufacturer and (Francis, 2021), the reading accuracy is 0.1 µgal with a standard deviation that can be less than 5 µgal, providing sufficient accuracy for possible future modelling work. The second advantage of this instrument is that it is easily transportable, enabling the acquisition of around forty gravimetric stations per day. The aim of these campaigns was to achieve accuracy in the order of tens of µgal while maintaining maximum mobility in the field. The topographic surveys were conducted using the GNSS antenna SXblue Premier RTK II (RTK option). A connection to the WALCORS GNSS network (WALlonia Continuously Operating Reference System) is ensured by the field controller. This enables RTK corrections (via the NTRIP protocol) to achieve horizontal and vertical accuracies of less than one centimetre.

2.2.2 Design of the campaign

The design decisions for this gravimetric campaign consist in defining the location of the gravimetric stations, the spatial sampling between them and the acquisition parameters. In general, the gravimetric stations follow the seismic lines of former seismic acquisitions mentioned above. To ensure a certain consistency in the spatial sampling used by these two geophysical methods, a spatial distribution of 50 m between gravimetric stations was chosen, the same distance observed between the vibration points of the seismic acquisition campaigns. The topographic survey of the stations was carried out with centimetre accuracy thanks to the corrections made by the WALCORS network. Latitude, longitude and altitude were measured in the WGS84 geographical coordinate system (EPSG:4326) and reprojected in the Lambert 1972 projected coordinate system (EPSG:31370), as shown in the map axes of this work. The EPSG acronym refer to IOGP's EPSG Geodetic Parameter Dataset.

The MoreGeo 2019-2022 campaign was divided into two main surveys. The first, in 2019, follows the Hainaut2019 seismic lines (Dupont, 2021) and covers the "Cœur du Hainaut" area with 5 north-south lines about 20 km long. This 2019 survey includes a total of 1726 stations, giving a cumulative line length of approximately 86 km. The second survey, carried out in 2022, was launched in the same region with the aim of collecting a set of data to complement the 2019 surveys. This new acquisition survey lasted about 6 months and included two lines running north-south along the Mons2012 seismic lines (Dupont, 2021) and three lines running east-west. This survey includes a total of 2456 stations representing approximately 123 km of acquisition. Figure 3 illustrates the location of the 2019 lines (in blue) alongside those of 2022 (in red). A major constraint in preparing the campaign was to avoid major roads and densely populated areas to move away from sources of vibration, resulting in better quality, low dispersion acquisitions. Hence, most stations are located along RAVeLs (autonomous network of non-motorised paths), towpaths and little used paths. However, three areas along the lines I, III and IV was not be covered by gravimetric acquisitions because of densely forested areas where the accuracy of the topographic surveys could not be achieved. Finaly, the new dataset of MoreGeo consists in 13,000 relative gravimeter readings in 4200 gravity stations spread over an area of 820 km².

https://doi.org/10.5194/egusphere-2026-3978
Preprint. Discussion started: 24 September 2026

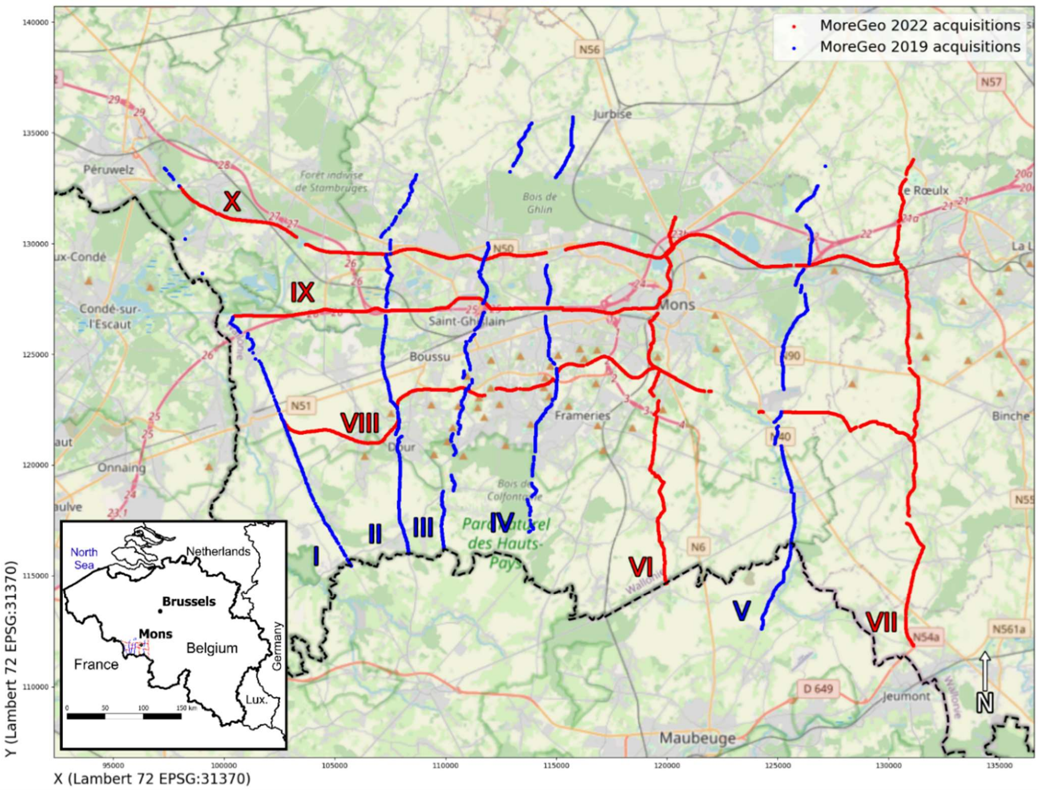

Figure 3 : Lines from the MoreGeo 2019-2022 gravity campaign, with the 2019 acquisition lines in blue and the 2022 acquisition lines in red. ©OpenStreetMap Distributed under the Open Data Commons Open Database License (ODbL) v1.0.

In terms of acquisition parameters, the number and duration of the acquisition cycles carried out at each station have been defined as three consecutive recording cycles per station, with a duration of 30 seconds for each cycle. At the end of each cycle, the mean, standard deviation, and standard error over a set of 30 measurements are recorded. Gravimeter readings are accepted via a repeatability criterion of less than 10 µgal for the three records. The levelling tolerance of the instrument was set at 10 arcseconds. In practice, the gravimetric survey was conducted using a daily step method inspired by the "step method (d)" described by Schüler (2000); the first two and last two stations of each day were visited at least twice. To monitor data acquisition quality between 2019 and 2022 and to facilitate the evaluation of the instrumental drift, a global resampling was achieved in October 2022 where 3% of all stations (i.e. 120 stations) were resampled. These stations were selected semi-randomly to ensure a good distribution of stations along acquisition lines.

2.2.3 The MoreGeo 2019-2022 gravity network pre-processing

Following the acquisition campaign, operations were initially performed including data filtering, outlier detection by following standards and the application of a two instrumental corrections. Data filtering and outlier detection focused on the accuracy of the gravimetric measurements (maximum standard error value for each recording cycle and average repeatability of less than 10 µgal for each acquisition cycle) as well as on the geographic and altimetric positioning of the stations. As a result of all this, the MoreGeo 2019–2022 data acquisition campaign has compiled a new dataset of gravimetric measurements acquired at 3,784 gravimetric stations. The Scintrex CG-6 Autograv™ internally evaluates four corrections: temperature, instrument tilt, tides and spring fatigue. In this work, only the first two corrections ($C_{Temp.}$ and C_{Tilt}) were retained. The tidal correction (C_{Tide}) was evaluated retrospectively (Section 2.2.4) to control the tidal model to be applied. The instrumental drift ($C_{Instrumental\ drift}$) has been evaluated in Section 2.2.4.

https://doi.org/10.5194/egusphere-2026-3978
Preprint. Discussion started: 24 September 2026

2.2.4 Temporal effect corrections

To evaluate the temporal effects affecting the gravimeter, acquisition loops (inspired by Schuler (2000)) and base stations (as in Rubio et al. (2022)) were also included in the design of the MoreGeo campaign. These base stations are at 'rue du Joncquois' in Mons. This site was chosen to minimise the impact of possible environmental changes, particularly the hydrogeological effects. It is free of vegetation, the thickness of the unsaturated zone is less than two metres, and the water level is very stable. As part of the MoreGeo 2019–2022 campaign, two effects must therefore be corrected prior to an absolute gravity referencing, the tide and instrumental drift effects. The total correction budget (**C**$_t$) required to determine the corrected ith reading r_i from the gravimeter reading $\tilde{r}_i$, is therefore expressed as:

$$r_i = \tilde{r}_i - C_{t,i}$$
$$where: C_t = C_{Temp} + C_{Tilt} + C_{Tide} + C_{Instrumental\ drift} \quad (11)$$

The first temporal effect affecting relative gravimeter readings that needs to be eliminated is the tide phenomenon. In practice, there are models for calculating this effect as a function of the latitude and longitude of the measuring station and of time. Many theoretical tide models have been tested for this paper such as Longman (1959) and all the models available with the Python library PyGTide, a Python wrapper for ETERNA PREDICT 3.4 (i.e. Hartmann and Wenzel (1995), Tamura (1987), etc.). The software Tsoft for Earth tide analysis, developed by the Royal Observatory of Belgium (Van Camp and Vauterin, 2005) has also been tested. More specifically, we used the gravimetric tidal parameters (amplitude factors δ and phase leads κ) related to the solid Earth tide and the ocean tidal loading specific to the Membach site of the international GGP/IGETS network located 145 km from Mons. These parameters capture the actual tidal effects at and around Membach, including local effects that pure theoretical models do not account for. This empirical model was selected because it reduced the average dispersion at the three stations of the MoreGeo campaign after removing all temporal effects. An associated error ε_{Tide} of 1.2 µgal was evaluated for this correction (cf. details in Appendix B.1).

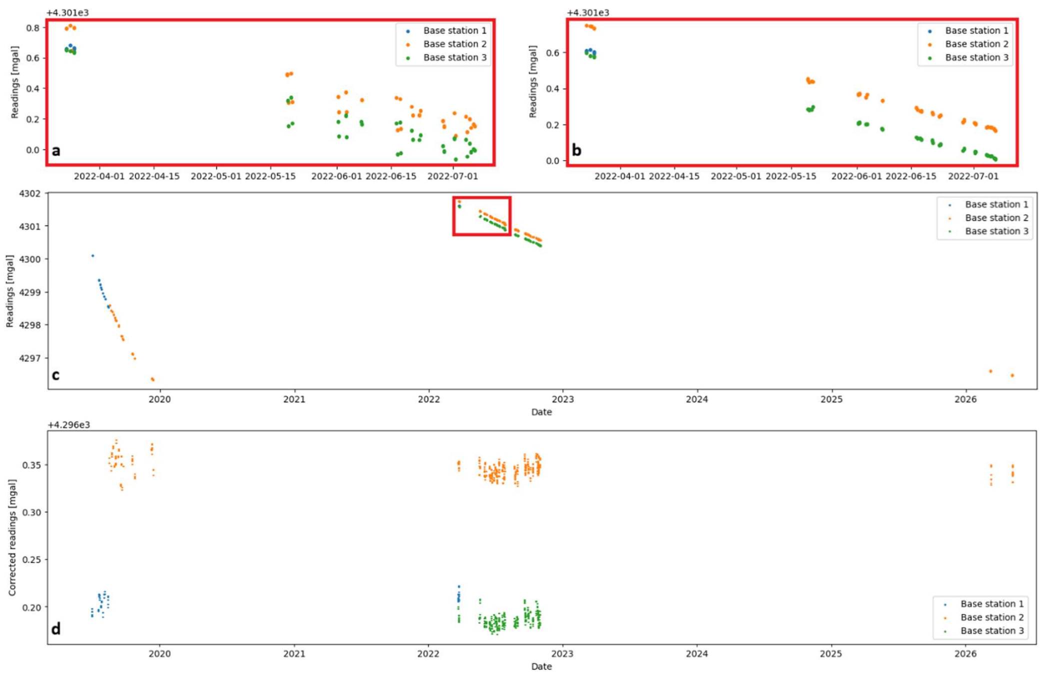

Figure 4: Readings (a) and corrected tide readings (b) at the MoreGeo base stations during the acquisition of profile VIII. Corrected tide readings (c) and corrected readings after the instrumental drift correction (d) at the MoreGeo base stations during the whole acquisition campaign period and during the absolute referencing of 2026.

https://doi.org/10.5194/egusphere-2026-3978
Preprint. Discussion started: 24 September 2026

Standard practice used in gravimetric acquisition is to choose a fixed base station for the duration of the campaign or absolute reference points to assess a daily drift correction by taking measurements at the beginning and end of each day. However, as MoreGeo was carried out in two phases (2019 and 2022) by different operators, base stations used on this site varied depending on the phase and the operators. Therefore, a solution, detailed in Appendix B.2, was implemented that integrated all stations visited more than once at different times (=closing loops). The instrumental drift function is then estimated using all these station loops via a Moving Weighted Least Squares (MWLS) algorithm across different acquisition periods. The optimal number of periods is determined using the Akaike Information Criterion (Akaike, 1974) and its derived form, the Bayesian Information Criterion (Wit et al., 2012). Once the drift has been corrected within these periods, they are aligned with one another using a method that combines a modified Depth-First Search algorithm (Tarjan, 1972)—with backtracking for closed cycles—and the least squares approximation using the Moore-Penrose pseudoinverse. In the end, the reference period chosen is the one that includes the corrected readings at the three bases of the campaign with the least dispersion. In the case of MoreGeo, this was the one that includes the resampling period at the end of October 2022. The dispersions, symbolised by the standard deviation of the corrected relative gravimeter readings at each of the three bases during the MoreGeo 2019-2022 campaign, are 8.9, 6.7 and 8.7 µgal, which is below the target accuracy of 10 µgal (Fig. 4). An associated error ε_{Drift} of 8.9 µgal was retained for this correction.

2.2.5 The MoreGeo absolute gravity referencing

To ensure that corrected gravimeter readings (r_i) of the MoreGeo network are referenced to absolute gravity, it is necessary to include absolute gravity references in the campaign. Since the authors did not have an absolute gravimeter, they had planned to perform a calibration using an absolute gravimeter belonging to the ROB. However, circumstances did not permit this. Regarding the surrounding gravimetric stations in the ROB and BRGM databases, all consist of data from relative gravimetric surveys that were subsequently referenced to absolute gravity, and most of them date back to the 1960s. Using these stations for absolute referencing is feasible but nevertheless carries a significant risk of bias. These risks stem from uncertainty regarding the data, the absolute referencing performed at the time for each of the historical campaigns included in the database and, above all, the imprecise positioning of the closest Belgian campaigns mentioned in Sect. 2.1. In addition, biases may result from regional mining subsidence that has occurred since the 1960s and may have slightly altered the elevation of certain stations. With the help of the Royal Observatory, the authors therefore developed an alternative approach, based on measurements from known Belgian absolute gravimetric stations (Campeol et al., 2026).

In 2026, the geodesic vertices at Werpin, Rochefort and Sohier have been surveyed by the Scintrex CG6. These reference stations are listed in the BGI database (https://bgi.obs-mip.fr/data-products/gravity-databases/absolute-gravity-data) and were regularly measured using an absolute gravimeter by the ROB or by Professor Olivier Francis of the University of Luxembourg until 2024 (Hendrickx M., personal communication). These measurements were integrated into the MoreGeo network through the realization of pre- and post-measurements at numerous 2019 and 2022 stations, covering all profiles. The basic equation of relative gravimetry with absolute reference is defined as:

$$g_P = g_{ref} + \alpha[r_P - r_{ref}] = g_{ref\,1} + \frac{g_{ref\,1} - g_{ref\,2}}{r_{ref\,1} - r_{ref\,2}}(r_P - r_{ref\,1}) \qquad (12)$$

Where $g_{ref\,1}$ and $g_{ref\,2}$ are the absolute reference gravity values, α is the scale factor (estimated as an average of $\alpha \equiv 1.001$ [mgal/Counter Unit]) and $r_{ref\,1}$ is the corrected gravimeter reading at the absolute reference station. The respective vertical gravimetric gradients of the three absolute reference stations were used to estimate the g_{ref} values for these stations at the same elevation as that of CG6. After averaging retained and corrected readings by station, Eq. 12 was used to establish the absolute referencing for the MoreGeo network. Results are shown in Fig. 5 with the map (a) and a south-north section (b) of the absolute gravity referencing of MoreGeo 2019-22 dataset compared to the ROB and BRGM databases.

Discussion about the error of the MoreGeo gravity dataset has to be done, taking into account all sources of uncertainty, whether related to the measurement campaign or to the processing steps. In the context of MoreGeo and the gravimetric processing described above, the mean square error of the MoreGeo readings ε_{r_P}, is calculated with Eq. 13:

$$\varepsilon_{r_P} = \sqrt{\varepsilon_{Survey}^2 + \varepsilon_{Drift}^2 + \varepsilon_{\mathrm{Tide}}^2} = 13.44\ \mu gal \qquad (13)$$

$\varepsilon_{\mathrm{Survey}}$ is the imprecision associated with the measurement of the anomaly. As a reminder, the precision aimed for by the

https://doi.org/10.5194/egusphere-2026-3978
Preprint. Discussion started: 24 September 2026

Scintrex CG-6 is of the order of 5 µgal (cf. Sect. 2.2.1). In practice, the value chosen during the acquisition campaign was 10 µgal (cf. Sect. 2.2.2) which corresponds to the repeatability of measurements obtained by operators on the field. ε_{Drift} and ε_{Tide}, discussed in Sect. 2.2.4 are respectively evaluated at 8.9 µgal and 1.2 µgal. Given that the maximal error on a g_{ref} is $\varepsilon_{g_{ref}}$(= 1.6 µgal) and letting $N = g_{ref\ 1} - g_{ref\ 2}$, and $D = r_{ref\ 1} - r_{ref\ 2}$, the mean square error made on g_P associated with a station P of MoreGeo gives by quadratic propagation:

$$\varepsilon_{g_P} = \sqrt{\left[\left(1+\frac{\Delta r}{D}\right)^2+\left(\frac{\Delta r}{D}\right)^2\right]\varepsilon_{g_{ref}}^2+\frac{N^2}{D^2}\left[1+\left(1+\frac{\Delta r}{D}\right)^2+\left(\frac{\Delta r}{D}\right)^2\right]\varepsilon_{r_P}^2} \qquad (14)$$

Based on this equation, the error therefore depends directly on the choice of reference stations. The ratio Δr/D must be minimized; thus, the larger D is relative to |Δr|, the smaller the error. For this reason, the Sohier and Werpin stations were selected, resulting in an error range of 41.9 µgal to 67.5 µgal depending on the specific MoreGeo station considered. Compared to the initial accuracy target of 100 µgal, this result yields a very satisfactory uncertainty. The error associated with each MoreGeo station is shown on the mini-map in the lower-left of Fig. 5a.

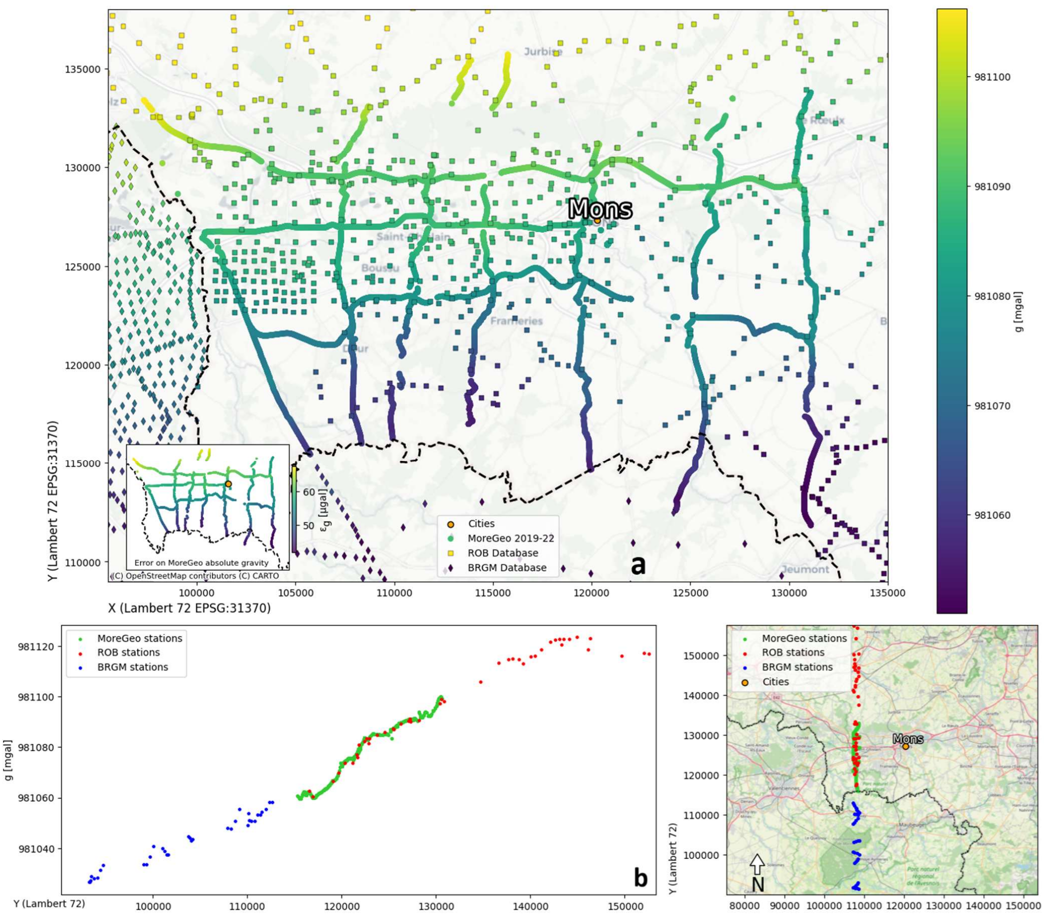

Figure 5: Absolute gravity referencing map of the MoreGeo 2019-22 dataset compared to the ROB and BRGM databases and the mean square error associated with MoreGeo stations (a). ©OpenStreetMap Distributed under the Open Data Commons Open Database License (ODbL) v1.0. MoreGeo 2019-22, ROB and BRGM absolute gravity data along a south-north section between Aulnoye-Aymeries (France) and Lessines (Belgium) (b).

https://doi.org/10.5194/egusphere-2026-3978
Preprint. Discussion started: 24 September 2026

2.3 The Battaille 1967 acquisition campaign retro-processing

The Battaille 1967 dataset contains the results of a gravimetric survey conducted by the CGG on behalf of Battaille Frères society in 1967, which is not included in the ROB database. The documents relating to this dataset are scarce. No documents relating to this campaign seem to have been preserved in the CGG archives (Dupont, 2021) and only a campaign report and the final map of the simple Bouguer anomaly calculated at the time were found in the archives of the Belgian Geological Survey. However, this survey was part of a broader data acquisition campaign carried out by the same company, which notably included the Battaille 1968–1969 survey, available in the ROB database under the *Extension 1948* (1972) campaign (Sect. 2.1). In this sense, integrate the Battaille 1967 campaign into the regional mapping of the gravity anomalies and disturbances is also an original aspect of this work, especially since it covers areas that have been poorly sampled.

The simple Bouguer anomaly obtained in 1967 was calculated using a simple Bouguer reduction, with a reduction density of 2.1 g cm^{-3}. To recover $\mathbf{g_P}$ from these $\mathbf{\Delta g_B}$ values, it is necessary to back-process the anomaly using the principles presented in Eq. 2, 4, 5, 7, and 9. However, three major issues arise at this stage. The first concerns the elevation coordinates of the stations, which could not be found in the archives even though they are essential for evaluating $\mathbf{A_B}$, $\mathbf{F}$ and $\boldsymbol{\gamma}$. To resolve this, the elevation from the 1m² resolution DTM used for the local topographic correction in the Sect 3.1 were employed. However, it is necessary to ensure that the elevation of these stations and the surrounding topography has not changed in 60 years. However, the Mons region experienced significant subsidence during the 20th century due to the coal mine activity (Ghiste and Albert, 1980; Leroy, 2014). Stations located within the area likely to be affected by mining subsidence must be excluded. These areas are defined by the extent of the mining zones mapped in (Delmer, 1977), with a 1-km buffer zone around them. This buffer takes into account the maximum depth of the mining concessions around this zone (1,000 m) and an angle of influence of 45°, which corresponds to the worst-case scenario regarding the impact of mining subsidence (Piguet, 1997).

The second issue concerns the geographic coordinates from Battaille 1967. These were obtained by georeferencing the anomaly map. Although the consistency of the station locations with historical paths and roads was checked station by station, there is likely still some few uncertainties in the positioning that cannot be resolved. Nevertheless, the need to include this survey to fill in the large, poorly sampled areas and the fact that it is located at the southern edge of the area of interest rather than at its center are two good reasons to incorporate Battaille 1967 into this study. Given this positioning issues and the elevation issue discussed above, it was decided to exclude stations located in areas where the topography varies significantly within a 150-meter radius. Finally, the last problem stems from the geodetic reference frame and the normal gravity model used at the time to calculate $\mathbf{\Delta g_B}$. Indeed, ensure the consistency with the legacy gravity data is primordial, such as respecting conventions of reducing the data sets. The models applied to the Battaille 1968–1969 dataset to estimate $\mathbf{\Delta g_B}$ in the 1960s were the normal height from the DNG altimetric reference system (epsg:5710) and the normal gravity of the International Hayford Ellipsoid (Verbeurgt and Kazmierczak, Geodesy Service at the National Geographic Institute of Belgium, personal communication). Given the similarities between these two campaigns, these models were applied to the Battaille 1967 dataset. The $\boldsymbol{\gamma}$, $\mathbf{F}$ and $\mathbf{A_B}$ effect with a reduction density of 2.1 g cm^{-3} was removed to retrieve the gravity data. It should also be noted that the gravity data obtained were expressed in the Potsdam system. This means that the data are subject to a positive bias of ~14 mGal (Moritz, 1980), which was subtracted to obtain gravity values consistent with modern reference frames.

3 Maps of gravity anomalies and disturbances

3.1 Evaluate the topographic correction ($\mathbf{A_T}$)

There is genuine interest in implementing $\mathbf{A_T}$ to gravity measurements, since this correction has never been evaluated or applied before to a gravity dataset for gravity anomaly mapping in Belgium. Regional (Dupont, 2021; Minguely, 2007; Battaille, 1969; Battaille, 1967; Leclerc, 1960) and national (Everaerts and De Vos, 2012) gravity anomaly mappings have always applied a simple Bouguer reduction, deeming the topographical effect in the region to be negligible. In France, $\mathbf{A_T}$ has already been evaluated up to a distance of 167 km around the BRGM gravimetric stations (Martelet et al., 2002) and will therefore not be reassessed for these stations. This 167 km extension, proposed by (Bullard, 1936) as a reference extension, represents the optimum radius to be used in topographic corrections to minimise the effects associated with the curvature of the Earth (LaFehr, 1991). Another point: it is clear that the location and elevation of the stations must be specified with a high degree of precision to avoid introducing bias when estimating $\mathbf{A_T}$. The comments made in previous

https://doi.org/10.5194/egusphere-2026-3978
Preprint. Discussion started: 24 September 2026

sections on the data from Battaille 1967, *Extension 1948*, and *Mons 1960* surveys imply that they are not suitable for estimating a topographic effect. Only a simple Bouguer reduction $\mathbf{A_B}$ has been applied to them, since the elevation of these stations is the only coordinate that is, a priori, reasonably accurate. This section therefore aims to implement an advanced method that accurately evaluates the effect of large-scale topography only on the MoreGeo data (Campeol et al., 2024a).

The method used in this work is based on modelling the area using rectangular prisms and calculating the gravitational influence of each of these prisms at each station point of MoreGeo. This was achieved using algorithms developed by the Harmonica Python library (Fatiando a Terra Project et al., 2024). Modelling these prisms from the topography to a reference level, requires the use of a precise digital terrain model (DTM) extending up to 167 km around the gravity stations. As described in Sect. 1.2, the reference surface to be considered for prisms is a quasi-geoid for anomalies and a reference ellipsoid for disturbances. The accuracy aimed for by $\mathbf{A_T}$ obviously depends on the accuracy and sophistication of the DTM used. To use the most accurate DTM possible while optimising computational time and memory, the correction has been divided into two parts. The first is based on a 25-meter grid extended to 167 km, hereafter referred to as 'regional topographic correction ($\mathbf{A_{Reg.\ T}}$). The second one is called 'local topographic correction' ($\mathbf{A_{Loc.\ T}}$), based on a finer grid detailed to the meter and extended to 6.65 km around the stations. This principle is mentioned in Eq. 15, which summarizes the two components involved in calculating topographic correction.

$$\boldsymbol{A_T = A_{Reg.\ T} + A_{Loc.\ T}} \qquad (15)$$

The 25-meter resolution DTM extended to 167 km around MoreGeo (Fig. 6a), was generated using the following sources:

- The 2021-2022 1x1 m² DTM of Wallonia, whose reference coordinate system is EPSG 31370 (Lambert 72) and whose reference height system is the Second General Levelling of the Kingdom (EPSG:5710). The owner of the data is the Service Public de Wallonie (SPW).
- The 2004 DTM of Flanders 25x25 m² "DHM-Vlaanderen, raster, 25 m", whose reference coordinate system is EPSG 31370 (Lambert 72) and whose reference height system is the Second General Levelling of the Kingdom (EPSG:5710). Owner of the data: Agentschap voor Geografische Informatie Vlaanderen.
- European 1 arc second bathymetry, whose reference coordinate system is EPSG 4326 (WGS84) and whose reference height system is the European Vertical Reference Frame 2000 (EPSG:5730).
- The 25x25 m² "BD ALTI®" DTM of France, whose reference coordinate system is EPSG 2154 (Lambert 93) and whose reference height system is the Nivellement General de la France - IGN69 (EPSG:5720). The owner of the data is the Institut National de l'Information Géographique et Forestière (IGN).
- The Copernicus 1 arc second DTM whose reference coordinate system is EPSG 4326 (WGS84) and whose reference height system is the European Vertical Reference Frame 2000 (EPSG:5730).

Each of these source data was reprojected into a common geographic coordinate reference system using transformation grid and Pyproj python library (Snow et al., 2025): the Pseudo-Mercator projection (EPSG:3857). This choice was justified by the need to have a reference projected coordinate system valid over the entire DTM area without having excessive distortions. This projection is also mentioned in the axes of Fig. 6a, specifying the metre as a unit on this figure. Concerning the altitudinal coordinate reference system, all the DTMs were reprojected to the normal height of the European Vertical Reference Frame EVRF2000 (EPSG:5730) or the WGS84 ellipsoidal height. The EVRF2000 was chosen because it is the only European vertical system whose transformations are supported by Pyproj. Projections to more recent European reference frames (EVRF2008 and EVRF2019) were not implemented at the time of this work. Each DTM was then aligned and resampled on a regular 25-meter spatial resolution grid before being merged into the grid shown in Fig. 6a.

The second DTM (Fig. 6b) used for the local topographic correction corresponds to the minimum bounding box with a 6.65 km buffer around the gravimetric stations. The extent corresponds to the first 10 zones of Hammer's method (Hammer, 1939). This 1x1 m² elevation grid was constructed on the basis of the following sources:

- The Walloon 1x1 m² DTM of 2021-2022 (EPSG:31370+5710) with an altimetric accuracy of ±0.12 m.
- The France 1x1 m² DTM "RGE ALTI®" (EPSG:2154+5720) with an accuracy of ±0.2 m.

In terms of geographic and altimetric coordinate systems, the Belgian conic projection Lambert 1972 (EPSG 31370) was chosen this time to limit the deformations associated with the reprojection of the Walloon DTM on which most gravity

https://doi.org/10.5194/egusphere-2026-3978
Preprint. Discussion started: 24 September 2026

stations are based. This projection is also mentioned in the axes of fig. 6b, specifying the metre as a unit on this figure. The altimetric coordinate system chosen are EVRF2000 and the ellipsoidal height of the WGS84 system as before.

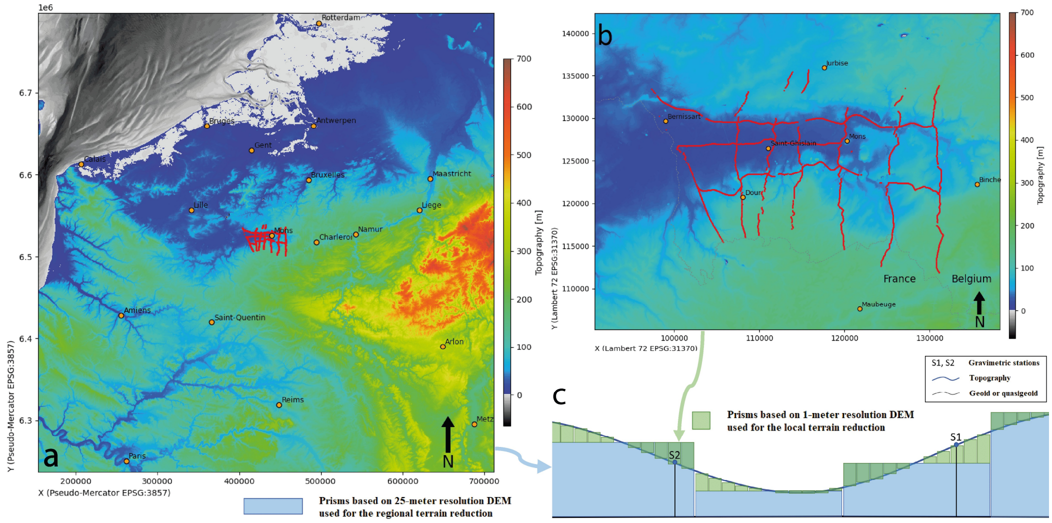

Figure 6: DTM extended to 167 km around gravity stations with 25x25 m² resolution (a). DTM limited to 6.65 km around gravity stations, resolution 1x1 m² (b). Schematic representation of the coupling between local and regional topographic correction (c).

Based on these two DTMs, rectangular prisms were constructed to perform the topographic correction as illustrated in Fig. 6c. The $\mathbf{A}_{\mathbf{Reg.\ T}}$ in Eq. 15 is based on the 25-meter resolution grid and generate the blue prisms in Fig. 6c, modelled between the reference surface and the DTM. The $\mathbf{A}_{\mathbf{Loc.\ T}}$ in Eq. 15 is based on the 1-meter resolution grid to generate the green prisms in Fig. 6c, modelled between the two DTMs. To properly compare the two grids, a subset of the the 25-meter resolution DTM, reduced to a 6.65 km extent, was projected into the EPSG 31370 coordinate system.

The prism method allows the possibility of integrating a numerical density model by assigning different densities to the prisms. This would be useful in the case of a sedimentary basin consisting of poorly consolidated and low-density deposits, as in the case of the Mons Basin. However, given the still significant uncertainties regarding the geometry of the basin floor and the densities, it was decided to use a simple constant-density model with a commonly used value of 2.67 g cm⁻³ for the 25-meter resolution prisms located above the reference surface. This value is generally used in gravimetry as it corresponds to the average density of surface rocks in a continental context (Hayford and Bowie, 1912; Hinze, 2003). 25-meter resolution prisms related to bathymetry, are assigned a density of -1.67 g cm⁻³. This is obtained by subtracting the bedrock density from that the water density, here approximated to be 1 g cm⁻³ (Vajda et al., 2008). In contrast, the density model assigned to the 1-meter-resolution prisms must ensure a certain degree of physical consistency according to the relative position of the two DTMs for each prism. The real topography, which is best approximated by the 1 m² DTM, is either above (S1 in Fig. 6c) or below (S2 in Fig. 6c) the surface of the 25x25 m² DTM. In the first case, the effect of these new prisms must be added while in the second case, it must be subtracted. Therefore, the density of these prisms may vary between four possible values, ±2.67 g cm⁻³ and ±1.67 g cm⁻³.

The station height to consider when calculating the gravimetric influence of the prisms for $\mathbf{A}_{\mathbf{Reg.\ T}}$ and $\mathbf{A}_{\mathbf{Loc.\ T}}$ has been set as the 1m-resolution DTM elevation. This choice is justified because, by definition, this correction is intended to account for the gravimetric effect of topography, which is modelled in greater detail by this grid. Numerical simulations examining the influence of a station elevation on this local topographic correction are available in Appendix C. The extent of the 1-meter resolution grid to be considered in $\mathbf{A}_{\mathbf{Loc.\ T}}$ can be reduced to improve computation time. Numerical simulations for station 10001 (available in Appendix C) have shown that the accuracy targeted by the correction is quickly achieved with a grid extending to a few hundred meters. Based on these simulations, the accuracy of the Scintrex CG6, and a reasonable safety margin, a 2-km extension around each station was chosen for this study.

https://doi.org/10.5194/egusphere-2026-3978
Preprint. Discussion started: 24 September 2026

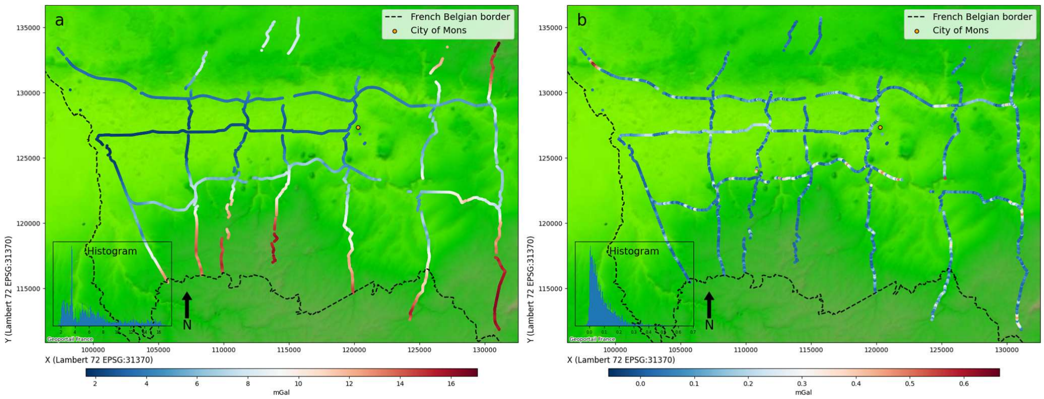

Figure 7: Regional topographic effect map with a reduction density of 2.67 g cm^{-3} and the 25 m resolution elevation grid extended to 167 km around the gravimetric stations (a). Local topographic effect map with a reduction density of 2.67 g cm^{-3} and the 25 and 1 m resolution elevation grids extended to 2 km around the gravimetric stations (b). Basemaps: National Institute of Geographic and Forest Information (IGN), Slope map (ELEVATION.SLOPES), WMTS service, https://data.geopf.fr, accessed on 2026-07-03.

Finally, the result of topographic correction is shown on Fig. 7 representing the regional and local topographic effects respectively on Fig 7a and Fig 7b. $\mathbf{A_{Reg.\,T}}$ presents a range from 1.62 to 17.04 mgal. This is quite similar to the simple Bouguer correction (between -1.67 mgal and -17.35 mgal) and the Bouguer spherical cap correction (between -1.69 mgal and -17.56 mgal) evaluated on MoreGeo data with a constant correction density of 2.67 g cm^{-3}. In terms of magnitude, the regional topographic effect is greatest in the northern and southern area of the zone where the altitude is highest, and the relief is less rugged. In the valley of the Haine river where the altitude is low (in the centre), the topographic effect is minimal as the $\mathbf{A_B}$ effect is also greatly reduced. On the Fig. 7b, the local topographic effect has minor importance, limited to a range between -0.05 and 0.66 mgal. Its influence is all the more significant in areas where the surrounding relief is strongly marked, such as in railway trenches (e.g. to the west of profile 10), near slag heaps, bridges and haul roads (encountered by lines 9, 10 and 8). This demonstrates the inability of the 25x25m DTM to capture all topographic features, such as bridge crossings, and the importance of correcting the topography with a more accurate DTM. It should be noted that the choice of station 10001 to assess the impact of the grid extent involved in the local topographic correction was a wise one, as it is located in the area where the effect seems maximum. The real terrain effect ($\mathbf{A_t}$) from Eq. 8 can be evaluated. The average is of -0.14 mgal and reaching up to -0.4 mgal. As supposed by previous regional gravimetric acquisitions mentioned above, values are quite small but not negligible. This is due to the large number of valleys, hills and other topographic features that reduce the norm of the gravity acceleration vector.

3.2 Compute the anomalies and the disturbances

With all the gravimetric data collected and before calculating the gravimetric anomalies and disturbances, a process was implemented to normalize the elevations of the various data sources by evaluating various elevation references. The hBG18 transformation grid (Slobbe et al., 2018) delivered by the Belgian National Geographic Institute (NGI) was used for conversions between ellipsoidal heights and normal heights in the DNG altimetric reference system (epsg:5710). The normal height of national reference system (DNG for ROB and MoreGeo and NGF-IGN69 (epsg:5720) for BRGM) were reprojected into the EVRF2000 elevation reference system (epsg:5730) using Pyproj python library (Snow et al., 2025). Following this, The MoreGeo gravity data were filtered by comparing their EVRF2000 elevation derived from the topographic survey and from the 1-meter-resolution DTM (Sect. 3.1). It should be noted that in the case of ROB and BRGM, the original station normal heights recorded at the time of acquisition and available in the databases, were used. To ensure consistency between the elevation used in the calculation of reductions and corrections applied to MoreGeo's anomalies and disturbances, the DTM's EVRF2000 height assigned to the stations was reprojected to DNG and ellipsoidal height using the same techniques as before.

https://doi.org/10.5194/egusphere-2026-3978
Preprint. Discussion started: 24 September 2026

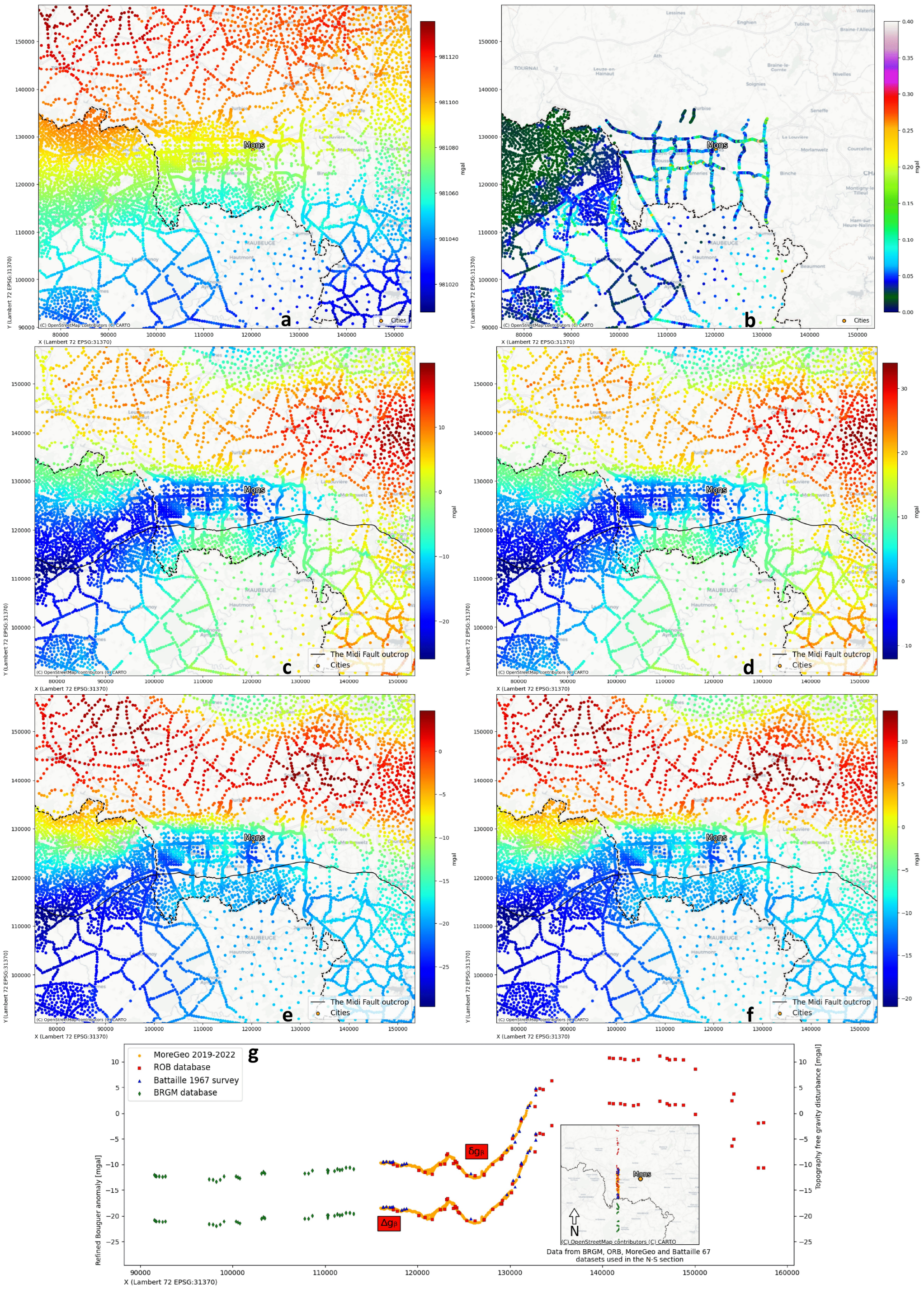

https://doi.org/10.5194/egusphere-2026-3978
Preprint. Discussion started: 24 September 2026

Figure 8: Observed Gravity data (a), Topographic effect of MoreGeo and BRGM datasets (b), observed Free-air anomaly data (c), observed gravity disturbance data (d), observed refined Bouguer anomaly data (e) and observed topography-free gravity disturbance data (f) in French-Belgian Hainaut. Refined Bouguer anomaly data and topography-free gravity data from the ROB database (in red), BRGM database (in green), MoreGeo 2019-2022 campaign (in orange) and Battaille 1967 survey (in blue) along a south-north section between Fayt-le-Franc and Lessines (g). Base map © OpenStreetMap contributors. ©OpenStreetMap Distributed under the Open Data Commons Open Database License (ODbL) v1.0.

By comparing the normal gravity derived from the WGS84 gravimetric model with the observed gravity data (Fig. 8a) and applying the appropriate corrections and reductions (as $\mathbf{A_t}$ shown in Fig. 8b), the Free-air anomaly $\boldsymbol{\Delta}\mathbf{g}$, the gravity disturbance $\boldsymbol{\delta}\mathbf{g}$, the refined Bouguer anomaly $\boldsymbol{\Delta}\mathbf{g_B}$ and the topography-free gravity disturbance $\boldsymbol{\delta}\mathbf{g_B}$ can be now extracted according to Eq. 2, Eq. 3, Eq. 9 and Eq. 10 respectively. These are represented in Fig. 8c-f. $\boldsymbol{\Delta}\mathbf{g_B}$ and $\boldsymbol{\delta}\mathbf{g_B}$ reflect only gravimetric variations related to the distribution of density in the subsurface, without taking into account topographic and altimetric effects. A south-to-north cross-section of these two quantities is shown in Fig. 8g, distinguishing among the four different data sources used in this work. To facilitate comparisons, the scale of values and colour bar are consistent with previous $\boldsymbol{\Delta}\mathbf{g_B}$ maps of Everaerts and De Vos (2012) (cf. Fig A1).

3.3 Gridding and interpolating

The 10187 unique gravity stations covering an area of 5000 km² must be interpolated to map the anomalies and the disturbances. Classically, interpolation methods such as inverse distance weighting or kriging methods (Dupont, 2021; Everaerts and De Vos, 2012) are used to interpolate gravity data onto a regular grid. However, in gravimetry, the three-dimensional nature of the observed phenomenon should be considered when mapping the anomaly. For this reason, the equivalent source method has been used in this work, as it allows for the consideration of 3D aspects through an inversion/direct modeling method (Dampney, 1969; Soler and Uieda, 2021; Fatiando a Terra Project et al., 2024). This method uses a process of least squares adjustment of point mass sources located beneath gravity stations. The depth of the sources is set and their density is adjusted to minimize, in a least squares sense, the difference between the observed data and the data simulated using a set of equivalent sources. In addition, this method needs to define the damping parameter controling the degree of fit between simulated data and observed data. This adjustment process therefore allows the noise to be smoothed by taking into account the uncertainty in the data.

To limit the number of sources involved and to reduce the computational time, the block-averaged equivalent source method introduced in (Soler and Uieda, 2021) and implemented in the Harmonica (Fatiando a Terra Project et al., 2024) library has been used. This block mesh also reduces the spatial aliasing caused by oversampling in a particular direction, especially that of the MoreGeo acquisition lines. In this work, a mesh size of 200 m was chosen, thus defining the resolution of the interpolation grid. To determine the optimum damping – source depth combination, 28 combinations of these two parameters were tested (damping → [0.1, 0.5, 1, 5], source depth → [1000, 1250, 1500, 1750, 2000, 2250, 2500]). The selection criterion was based on the evaluation of a chi-square (χ^2) criterion for the MoreGeo data (Eq. 17), since this is the data source for which the uncertainty was deemed the most reliable (Sect. 2.2.5). This criterion evaluates the average of the squares of the differences, weighted by uncertainty, between the observed data (f_i) and the simulated data (d_i). This statistical criterion is therefore preferable to the RMS (Eq. 16), as it allows to take into account the uncertainty of the data.

$$R^2 = \frac{1}{N}\sum_{i}^{N}(d_i - f_i)^2 \tag{16}$$

$$\chi^2 = \frac{1}{N}\sum_{i}^{N}\left(\frac{d_i - f_i}{\varepsilon_{g_P}}\right)^2 = \frac{\Phi_d}{N} \tag{17}$$

An initial adjustment of the equivalent sources was performed on this dataset. The optimal combination of parameters in terms of the MoreGeo χ^2 criterion is a depth of 1,250 m and a relatively low damping parameter of 0.5, regardless of the anomaly or disturbance used. The results of this initial adjustment revealed significant differences between the observed anomaly and the simulated anomaly at gravimetric stations from certain campaigns in the ROB database (see Fig. D1 in Appendix D). In particular, the *Dinant Basin* (1962), located southeast of the study area, consistently exhibits significant positive differences compared to the nearby *Philippeville* (2020) and *Central Belgium* (1996) campaigns. These observed differences reflect a constant shift estimated at 1.35 mgal, calculated based on 15 pairs of neighboring stations less than 100 m apart, including one station in the *Dinant Basin* (1962). This systematic difference could be indicative of errors made

https://doi.org/10.5194/egusphere-2026-3978
Preprint. Discussion started: 24 September 2026

either during its initial absolute calibration at the time or during its integration via retro-processing into the ROB database; however, these hypotheses could not be verified. Also, the *Extension 1948* (1972) and *Mons* (1960) campaigns show outliers with higher than average positive and negative differences, probably because these campaigns were older and therefore less accurate than the others. The MoreGeo data show very small or even almost no differences, proving that direct modelling by equivalent sources can explain these high-precision measurements.

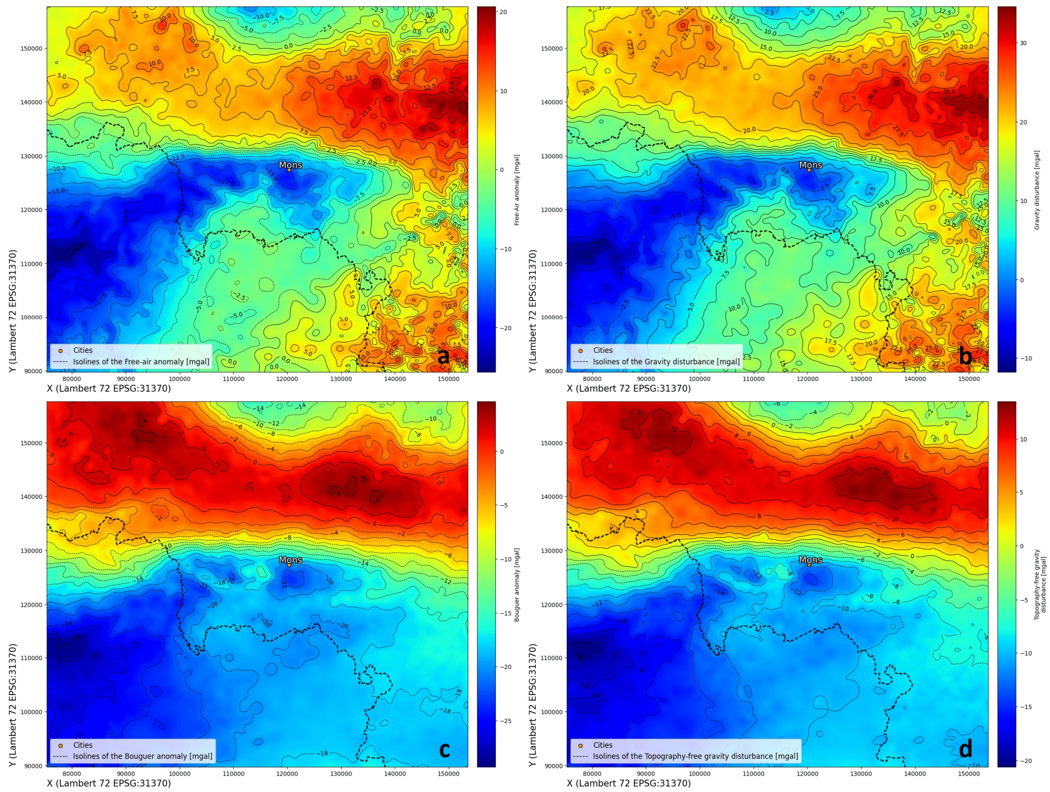

Figure 9: French-Belgian Hainaut Free-air anomaly map (a), gravity disturbance map (b), refined Bouguer anomaly map (c) and topography-free gravity disturbance map (d) gridded with 200-metre resolution and predicted by the block-averaged equivalent sources methodf A single large-format version of (c) and (d) is available in Appendices D3 and D4, respectively.

Based on these observations, a second phase of adjustment of the equivalent source model was realised, after shifting the *Dinant Basin* campaign (1962) and eliminating *Extension 1948* (1972) and *Mons* (1960) outlier stations (cf. Fig. D2). The outlier stations of *Extension 1948* (1972) and *Mons* (1960) are stations showing differences greater than 2 mgal between the observed and the simulated anomaly. The new optimal combination of parameters is an attenuation of 0.1 and an equivalent source depth of 1,250 m for the four anomalies and disturbances. After the adjustment phase, a prediction step is performed to interpolate the fields on the regular grid. The Fig. 9a-d show the Free-air anomaly map (a), the gravity disturbance map (b), the refined Bouguer anomaly map (c) and the topography-free gravity disturbance map (d). This represents one of the main results of this work. The gravimetric isovalue curves are plotted with a step of 2 mgal.

3.4 Interpretation and discussion

Based on these mappings, it would be interesting to propose an interpretation by comparing them to the regional geology. For clarity, these interpretations will be expressed only on the $\boldsymbol{\Delta g_B}$ and $\boldsymbol{\delta g_B}$ maps, since they are the most decorrelated from the topography. Figure 10a shows the isovalue curves of the $\boldsymbol{\Delta g_B}$ together with the simplified geological map of the region and the chronostratigraphic column. Figure 10b focuses on the Mons Basin area, where the isovalue curves of $\boldsymbol{\Delta g_B}$ are

https://doi.org/10.5194/egusphere-2026-3978
Preprint. Discussion started: 24 September 2026

plotted against the thickness map of the Meso-Cenozoic deposits, obtained from the Paleozoic top map of Dupont (2021).

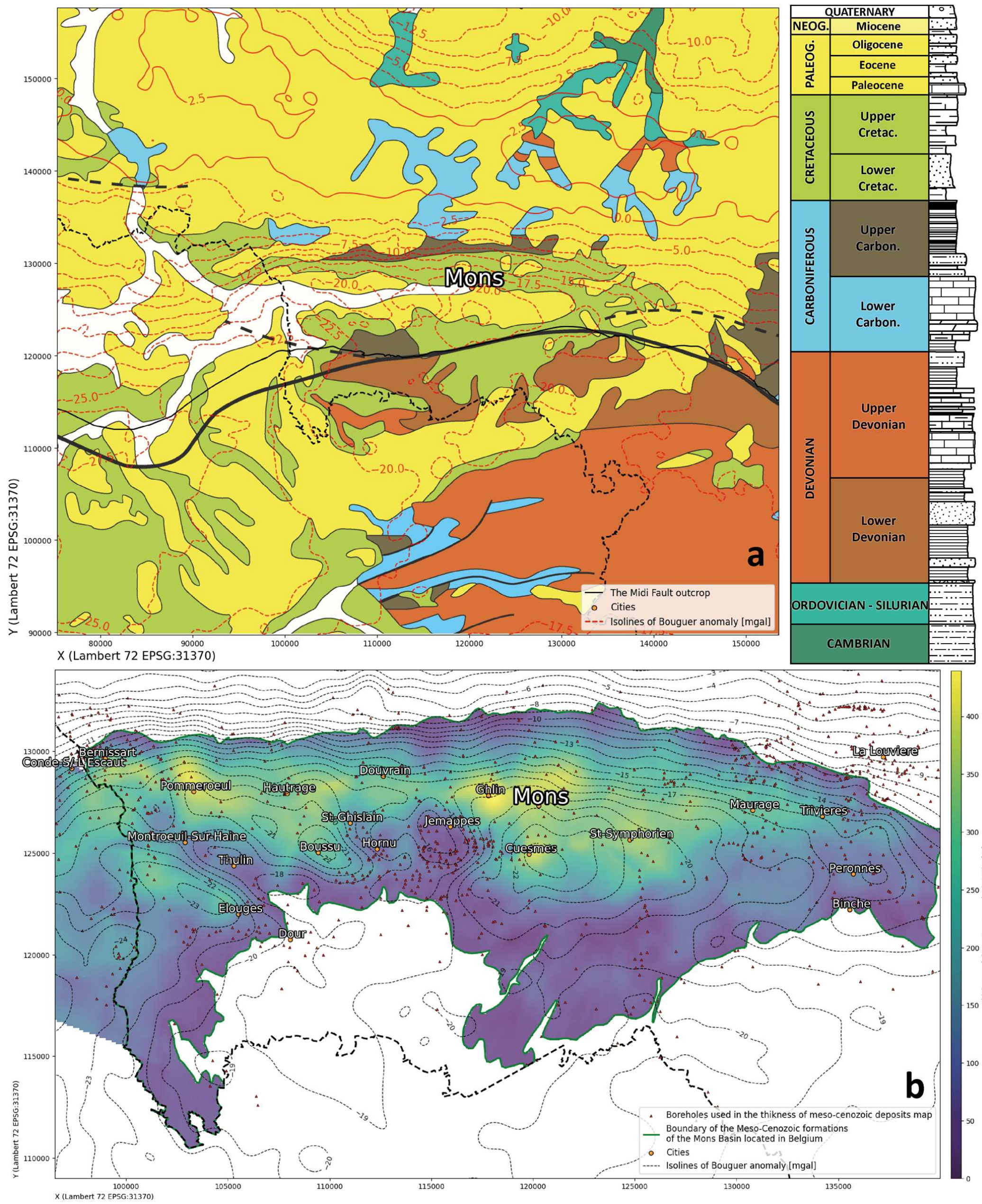

Figure 10: Iso-value curves of the refined Bouguer anomaly with the 1:1,000,000 geological map of France (Chantraine et al., 1996) modified and the chronostratigraphic column (a). Iso-value curves of the refined Bouguer anomaly on the thickness map of the Meso-Cenozoic formations of the Mons Basin, obtained from Paleo-Mesozoic unconformity well markers (Dupont, 2021) (b).

https://doi.org/10.5194/egusphere-2026-3978
Preprint. Discussion started: 24 September 2026

At first sight, the general appearance of the $\boldsymbol{\Delta g_B}$ and $\boldsymbol{\delta g_B}$ maps follow broadly the same trend as the maps of (Everaerts and De Vos, 2012) and (Minguely, 2007). A major south- north gradient extends from the west between Nieuport and Dunkirk to the east of Belgium. It is classically interpreted as the northward rise of very dense Palaeozoic pelitic sediments from the Ordovician-Silurian sedimentary cycle, which were folded during the Caledonian orogeny to form the Brabant Massif (Everearts and Devos, 2012; Mansy et al., 1999). This gravity gradient is currently the most reliable index for locating the Brabant unconformity at depth due to the lack of seismic reflectors. However, in the study area, to the north of the Mons Basin, the gradient is particularly steep, probably due to the combined effects of the steep uplift of these dense pre-Silurian terranes due to a tectonic wedging effect during the Variscan thrust (Mansy et al., 1999) and the thick Meso-Cenozoic sediments of the Mons Basin (Everaerts and Hennebert, 1998). According to (Everaerts and Hennebert, 1998) this gradient could also be related to the presence of the hypothetical Bordière fault. This large dextral strike-slip fault outcrops to the east of Belgium and is still thought to underlie the Mons region. Its vertical displacement would accentuate the subsidence of the Mons basin (Legrand, 1968).

To the north of the area, near the towns of Braine-le-Château and Lessines, the maps show the beginning of the negative Brabant anomaly, which lies directly beneath the Cambrian core of the Brabant Massif. This well-known anomaly on the Belgian gravity maps, has been interpreted in (Hennebert, 1993; Mansy et al., 1999) as the signature of a succession of deep, arc-shaped granitic batholiths, elongated in the direction of the massif and forming a rigid crustal basement. This characteristic negative anomaly was used in (Herbosch and Debacker, 2018) to map the Brabant Massif under Meso-Cenozoic cover, in particular by highlighting the Asquempont detachment system (Debacker et al., 2001; Debacker et al., 2004). The southern part of the maps, in French Hainaut (the Avesnois region), looks more like a vast gravimetric trough with a fairly gentle east-west gradient. This area lies on the edge of the Paris Basin overlying the Palaeozoic terrains of the Ardennes Allochthon (Belanger et al., 2012). This trend is therefore mainly explained by the thickening of the Meso-Cenozoic deposits and the deepening of the Palaeozoic top towards the west (Minguely et al., 2006; Mansy et al., 1999). In fact, the synclinal and anticlinal folding structures affecting the Carboniferous and Devonian formations of the Ardennes allochthon do not present sufficiently high-density contrasts in this region.

A more complex dynamic, characterized by both negative and positive anomalies are prominent in the centre of the maps. In (Dupont, 2021; Everaerts and Hennebert, 1998; Battaille, 1967), these have already been attributed to variations in the thickness of the Meso-Cenozoic deposits by correlating the gravity isovalues with the isohypses of the Paleozoic basement. However, it is now possible to constrain the lateral extent of structures affecting the basement by comparing them explicitly with the thickness map of the Meso-Cenozoic deposits in Fig. 10b. This figure also shows the location of the towns and villages from which the eponymous structures listed below take their names. This thickness map has been generated from the cubic spline interpolation surface of the Paleo-Mesozoic unconformity well data published in (Dupont, 2021) and the 1-meter resolution DTM of this work. It should be noted that this thickness map does not include geophysical information.

This overlay shows that the positive and negative gravity anomalies are clearly correlated with the thickness of the Meso-Cenozoic sediments and the relief of the Paleozoic and Meso-Cenozoic unconformity. To the west, two vast, enclosed depressions (or basins) with a very thick sediment layer form the contours of the "*Sillon d'Élouges"* on one side and the "*Cuves de Pommeroeul, Herbières (Hautrage) et Boussu"* on the other (Everaerts and Hennebert, 1998; Delmer and Van Wichelen, 1980). The raised or domed areas that separate these 'basins' can also be divided into two elevated entities: the "*Surélèvement de Montroeul-sur-Haine - Thulin - Boussu-Bois"* (south-east) and the "*dôme d'Hensies"* (north-west). This Southeast of Bernissart structure is in an area that was free of any gravimetric acquisition until 2019. The relief of the top of the Palaeozoic basement in this area forms well-defined a positive relief that has long been mapped (Cornet and Stevens, 1921-1923; Stevens and Marlière, 1944). This is oriented along an axis N130°E, which belongs to the family of main directions N125-145°E of this Meso-Cenozoic unconformity highlighted in (Licour, 2012; Dupont, 2021).

In the centre of the basin, the "*Dômes d'Hornu et de Jemappes"* form a distinct positive anomaly in the $\boldsymbol{\Delta g_B}$ map. The Douvrain basin to the north of these domes is not particularly visible, but it is very likely that the extension of the -17 mgal isovalue in this area of the map is related to the coupled effects of this basin and the proximity of the Palaeozoic outcrop to the north. To the east of this zone, the *Cuves de Cuesmes, Mons and Saint-Symphorien* clearly cause the largest negative anomaly on this map (Dupont, 2021; Everaerts and Hennebert, 1998). At the eastern edge of the basin, more precisely to the north and north-west of Binche, the extension of the -18 and -17 mgal isovalues also appears to be limited by the local overthrusts induced by the *Cuves de Péronnes, Trivières* and *Maurage*.

4 Conclusion

Three areas of improvement have been studied in this work to present the updated refined Bouguer anomaly map and the new free-air anomaly, gravity disturbance and topography-free gravity disturbance maps:

- The acquisition and the integration of the new MoreGeo 2019-2022 gravimetric acquisition campaign, characterised by a high spatial sampling rate, a full control of the gravimetric processing chain and a low root mean square error range of 41.9 µgal to 67.5 µgal depending on the station;
- The integration of the old data from the Battaille 1967 campaign and its retro processing based on historical anomaly data respecting the historical geodetic and ellipsoidal models.
- The evaluation of topographic correction - a first for Belgian regional data;

These improvements have enabled to produce maps with a 200-meter resolution and with a much larger number of measurements distributed more evenly throughout the entire area. The impact on the quality and accuracy of these maps is therefore considerable, making it much more suitable for regional studies. All the observations and interpretations made on the maps are very consistent with the geology, and particularly the shallow geology of the Mons and Paris sedimentary basins. They allow to locate and to map the main structures affecting the Paleozoic basement under cover. This work — and particularly the data collected — therefore constitutes an important key for future geological modelling projects, especially that of the Carboniferous limestones of the Brabant Parautochthon, for which the effect of the Meso-Cenozoic must be accounted for. It should also important to note that the implementation of these future modeling and direct inversion studies must be systematically accompanied by an assessment of gravimetric error, as was done for the MoreGeo data. In particular, this could be based on metadata (positioning and elevation errors) as well as errors related to the DTM's resolution.

Author contributions

OK supervised the acquisition of the financial support for the project leading to this publication. OK and QC conceptualised the research activities. OK, QC and ND planned the MoreGeo acquisition campaign. QC contributed to the MoreGeo acquisition and processed the data. QC and OK developed the gravimetric processing codes. QC and ND performed the compilation and the fusion of new acquisitions and legacy data. QC developed the method and evaluated the topographic correction. QC performed the maps and conducted the analysis of the results. QC prepared the manuscript and the figures. OK and ND reviewed and edited the manuscript.

Competing interests

The authors declare that they have no conflict of interest

Acknowledgements

This work is part of a PhD thesis funded by the University of Mons (Faculty of Engineering, Geology and Applied Geology Department).
The authors would like to thank the European Regional Development Fund for its financial support in the framework of the MORE-GEO project.
The authors are grateful to researchers Thomas Lecocq, Koen Van Noten, Marc Henrickx and Stefaan Castelein (Royal Observatory of Belgium), as well as researchers Jeffrey Verbeurgt and Elise Kazmierczak (National Geographic Institute of Belgium) for their invaluable assistance and the many discussions held regarding the absolute referencing of the MoreGeo 2019–2022 and Battaille 1967 surveys.
The authors thank researchers Franck Martin, Louis Christiaens and Ivan Nanfo Djoufack for their active participation in the MoreGeo 2019-2022 gravity acquisition campaign.
The authors would like to express their sincere gratitude the two anonymous reviewers who assessed the manuscript during its previous submission to EGUsphere in 2025 (egusphere-2025-497). Their feedback contributed significantly to the improvement of this work, raising it to a markedly higher standard.
DeepL Write has been used to improve the clarity and linguistic quality of this document. No content has been generated or modified beyond stylistic adjustments.

https://doi.org/10.5194/egusphere-2026-3978
Preprint. Discussion started: 24 September 2026

Appendices

Appendix A relative to Sect. 1

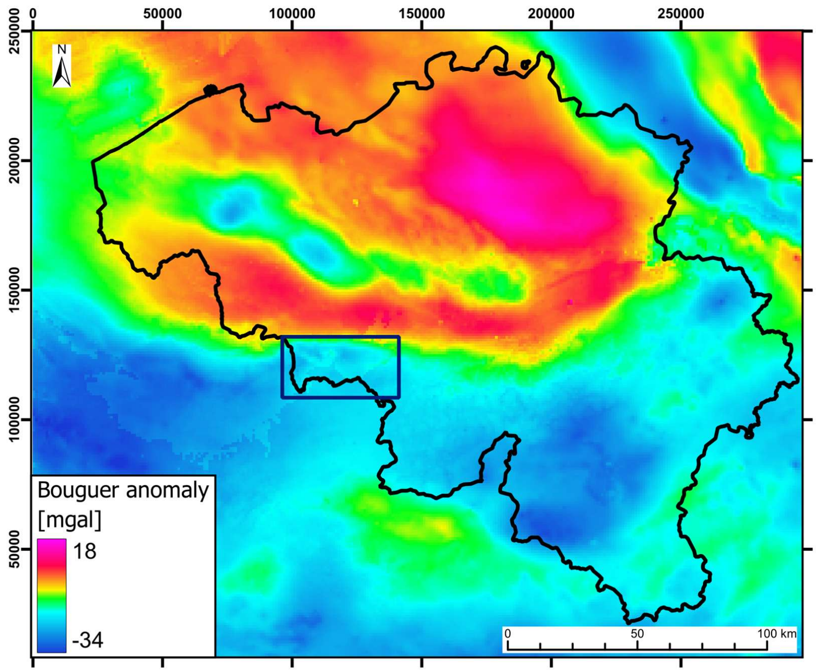

Figure A1: Belgian simple Bouguer anomaly map with a variable reduction density. Modified from (Everaerts and De Vos, 2012) to represent the extent of the study area.

Appendix B - Technical and theoretical developments of the MoreGeo readings temporal corrections (Sect. 3.1)

B.1 Comments on the Earth tide correction (C_{Tide})

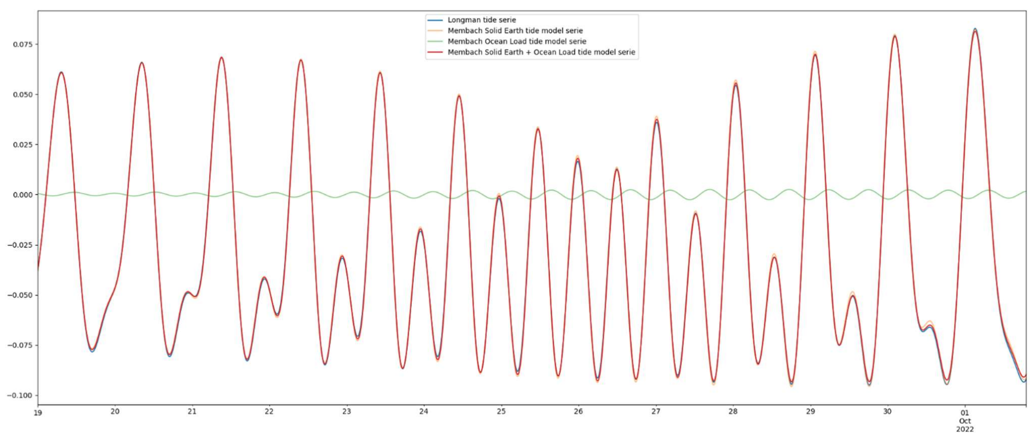

Figure B1: The Earth tide time-series effect (in mgal) computed over the period between 09.19.2022 and 10.01.2022 at one base station of MoreGeo. Longman (1959) tide model and Earth tide and Ocean load empirical response of Membach station from Tsoft software are compared.

Since Tsoft (like pygtide) provides time-series simulations of tidal effects at specific stations, it was decided to evaluate the error resulting from the use of a single time series for all MoreGeo stations. Three time series were simulated: one for the station at the southeastern end (ID: 7001), one for the station at the northwestern end (ID: 1448), and one for the most stable base station. Over the entire period from 2019 to 2026, a maximum difference of 1.2 µgal was observed between the time-series of the base station and the other two. The base station was chosen as the reference for the tidal effect time series, and an associated accuracy e_{Tide} of 1.2 µGal was chosen. Despite this approximation, the tidal effects corrected using Tsoft proved to be consistently more accurate than those obtained with theoretical models. Figure B1 shows the Earth tide time-series computed with the Longman (1959) tide model and Earth tide and Ocean load empirical models using Tsoft over the period between 09.19.2022 and 10.01.2022 at the base station of MoreGeo.

B.2 Instrumental drift correction developments ($C_{Instrumental\ drift}$)

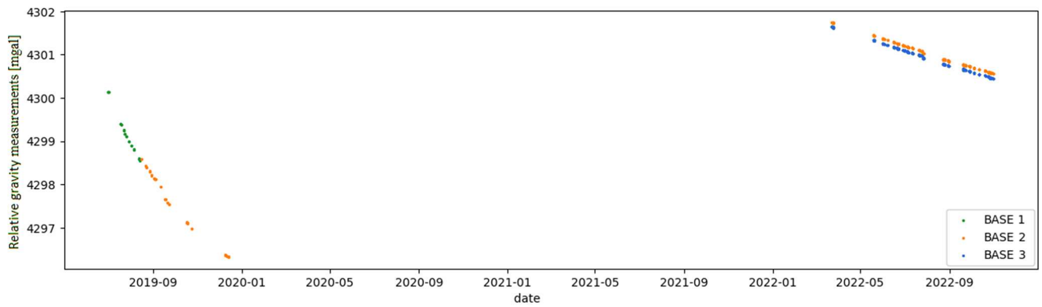

Figure B2: Estimated instrumental drift between 2019 and 2022 on raw relative gravimeter readings of the base stations.

This appendix comments in details the mathematical developments made to evaluate the instrumental drift affecting the gravimeter during the period covering the 2019 and 2022 acquisition phases. The instrumental drift is related to the technology of the measuring instrument. In the case of the Scintrex CG-6 relative gravimeter used for the MoreGeo 2019-2022 campaign, the technology used is a fused quartz spring system with electrostatic cancellation (Phillips, 2015; Francis, 2021) and the corresponding instrumental drift can be related to the gravimeter spring elongation over time. According to (Francis, 2021)**,** the drift of this instrument is quadratic and its growth decreases with time. In terms of magnitude, the manufacturer Scintrex estimates the range of daily drift between 0.02 and 0.2 mgal per day. Francis (2021) estimates the drift of the Scintrex CG-6 to be a few tens of µgal per hour. Figure B2 shown the instrumental drift initially estimated using only the base stations and highlights the different base stations used during the campaign. Due to the extended period of the MoreGeo campaign and the fact that base stations differ according to the acquisition phase and the acquisition operator, a new approach was adopted that used closing loops (cf. Sect. 2.2) to approximate the observed drift by a piecewise quadratic function over time.

The real evolution of the drift ($\Delta\tilde{r}(t)$) overt time can be estimated using closing loops made up of all pairs of records (separated by at least five minutes) from the same station that has been visited several times, either systematically or occasionally. The idea is to use all available information, not just the relative gravimeter readings taken at the base stations, to approximate the drift since some base stations were not used throughout the MoreGeo campaign. For example, the first base station was only used until August 2019, and some lines (notably the line 5) were acquired without systematically returning to the bases. Each loop linearly approximates the time variation of the readings ($\Delta\tilde{r}(t)\ \Delta t^{-1}$) that occurs over a time interval (Δt). Assuming a drift follows a quadratic law, the drift variation value is assigned to the centre of the time interval framed by the loop and evaluated by the secant in this interval. From the point of view of statistics and uncertainty calculation and if we assume that the average record $\tilde{r}^*$ made on n measurements $\tilde{r}_i$ (at least 30) by the relative gravimeter follows a normal distribution of the form:

$$\frac{\sum_1^n \tilde{r}_i}{n} = \tilde{r}^* \rightarrow N\left(\tilde{r}, \frac{\sigma}{\sqrt{n}}\right) = N(\tilde{r}, \varepsilon) \qquad (B1)$$

Considering there is no significant uncertainty about the time of measurement, the drift should follow a normal distribution:

https://doi.org/10.5194/egusphere-2026-3978
Preprint. Discussion started: 24 September 2026

$$\left(\frac{\Delta\tilde{r}}{\Delta t}\right)^{*} = \frac{\tilde{r}_2-\tilde{r}_1}{\Delta t} \to N\left(\frac{\Delta\tilde{r}}{\Delta t},\frac{\sigma_1+\sigma_2}{\Delta t\sqrt{n}}\right) = N\left(\frac{\Delta\tilde{r}}{\Delta t},\frac{\varepsilon_1+\varepsilon_2}{\Delta t}\right) \qquad (B2)$$

Since the true standard deviation of the distribution is unknown, the standard deviations associated with the two records , which are unbiased estimates of the variance, follow a Student distribution of the form:

$$s = \sqrt{\frac{1}{n-1}\sum_{i}^{n}(\tilde{r}_i-\tilde{r}^{*})^2} \to \tau_{(n-1)} \qquad (B3)$$

Thus, the error in estimating the drift in a loop, denoted ε, is a function of the sum of the standard errors of the two records used to calculate the drift and the Student's t coefficient for a given 1-α confidence level:

$$Confidence\ interval\ = \left[\tilde{r}^{*} - t_{\left(\frac{\alpha}{2}\right)}^{(n-1)}\varepsilon ; \tilde{r}^{*} + t_{\left(\frac{\alpha}{2}\right)}^{(n-1)}\varepsilon\right] \qquad (B4)$$

$$Confidence\ interval\ = \left[\frac{\Delta\tilde{r} - t_{\left(\frac{\alpha}{2}\right)}^{(n-1)}(\varepsilon_1+\varepsilon_2)}{\Delta t} ; \frac{\Delta\tilde{r} + t_{\left(\frac{\alpha}{2}\right)}^{(n-1)}(\varepsilon_1+\varepsilon_2)}{\Delta t}\right] = \left[\frac{\Delta\tilde{r}}{\Delta t} - \frac{t_{\left(\frac{\alpha}{2}\right)}^{(n-1)}(\varepsilon_1+\varepsilon_2)}{\Delta t} ; \frac{\Delta\tilde{r}}{\Delta t} + \frac{t_{\left(\frac{\alpha}{2}\right)}^{(n-1)}(\varepsilon_1+\varepsilon_2)}{\Delta t}\right] \qquad (B5)$$

After determining the station pairs and their associated drift variations over time ($\Delta\tilde{r}\ \Delta t^{-1}$) as a function of time, any station pairs that do not represent a plausible measure of instrumental drift due to external disturbance are removed (typically a measured drift above 1 mgal day^{-1}). External disturbance can be due to loud noise such as a passing vehicle during one of the records of the pair, a variation in the height of the tripod, incorrect levelling of the gravimeter, etc. Also, the maximum duration and position of the time interval between records within the same pair was filtered. Then, the filtered drift variations are used in a Moving Weighted Least Squares (MWLS) method to efficiently interpolate the drift variation over time. This MWLS performs a linear least squares interpolation that weights the drift variations data by their uncertainty within a moving window that moves forward daily. In this way, the drift at each time is evaluated by weighting the drifts only observed around that time. This method also avoids filtering station pairs with a very small-time interval because the error in the drift estimate (ε) becomes very large and these doublets therefore have little weight in the MWLS.

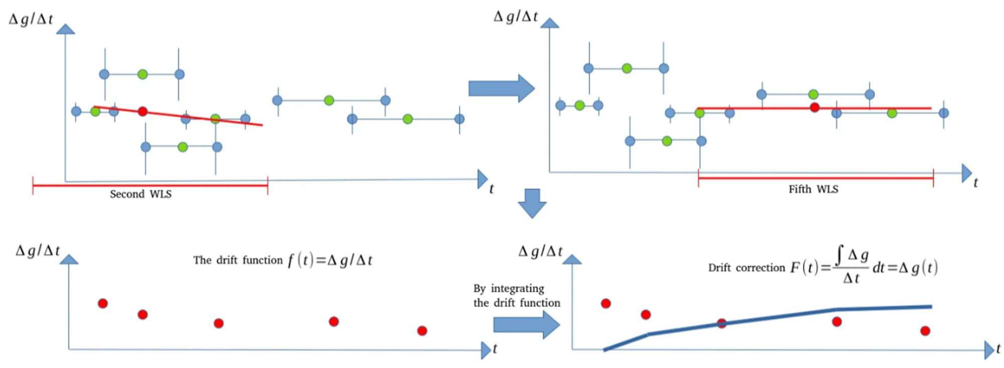

Figure B3: Illustration of the principle used to determine the drift function using Moving Weighted Least Squares (MWLS). The blue points are the two measurements associated with a closing loop represented by the green points. The red points are the result of the MWLS calculated from the green points.

In the MWLS, the parameter used is the width of the time window which can range from one day to one year to separate surveys 2019 and 2022 in the process. The value adopted is the optimum value which, after drift correction, give the least dispersion of the relative gravimeter readings at the three bases of the campaign. Figure B3 illustrates these principles. Next, the curve resulting from the MWLS and called the drift function is integrated from a reference date t_0 over time to give the drift correction to be applied to the relative gravimeter readings throughout the campaign period (cf. Eq. B6). This drift

https://doi.org/10.5194/egusphere-2026-3978
Preprint. Discussion started: 24 September 2026

correction therefore varies quadratically with time. This method inevitably reduces also the environmental effects on gravity encountered when using conventional methods to assess instrumental drift at single-site base stations.

$$\int_{t_0}^{t_1} \frac{\Delta\tilde{r}}{\Delta t}\,\mathrm{dt} = \Delta\tilde{r}(t) = \boldsymbol{C}_{\boldsymbol{Instrumental\ drift}} \qquad (B6)$$

For the MoreGeo gravity campaign, the total duration of the campaign was such that it was not possible to approximate the drift using a single drift function. The inconclusive result of this attempt, shown in the Fig. B4a, is majorly due to the shape of the long-term drift and its decay, which could not be modelled by a single quadratic function. This observation can be partly explained by the return of the gravimeter to the manufacturer in 2020, which probably influenced the shape of the drift between the two surveys of the campaign. It was therefore decided to determine two drift functions respectively for the 2019 and 2022 surveys. The result, shown in the Fig. B4b is much better than the previous one due to the lower dispersion of the relative gravimeter readings at the three base stations after the drift correction. Unfortunately, this dispersion within these two periods still exceeds the accuracy target of 10 µgal and does not meet the requirements of this treatment.

Nevertheless, it turns out that dividing the 2019-2022 MoreGeo campaign into periods in order to determine a single drift function within these periods significantly improves the result. However, dividing the MoreGeo campaign into an excessive number of periods would lead to an ever finer dispersion but a completely meaningless result. It is therefore necessary to determine the optimum number of periods where the number of parameters to be included in the drift model is most relevant in relation to the precision obtained. For this purpose, the Akaike Information Criterion (AIC) and its derived form, the Bayesian Information Criterion (BIC), have been evaluated. These criteria are defined with the Eq. B7 (Akaike, 1974) and B8 (Wit et al., 2012) respectively.

$$AIC = 2k - 2\ln(L) \qquad (B7)$$

$$BIC = \ln(n)\,k - 2\ln(L) \qquad (B8)$$

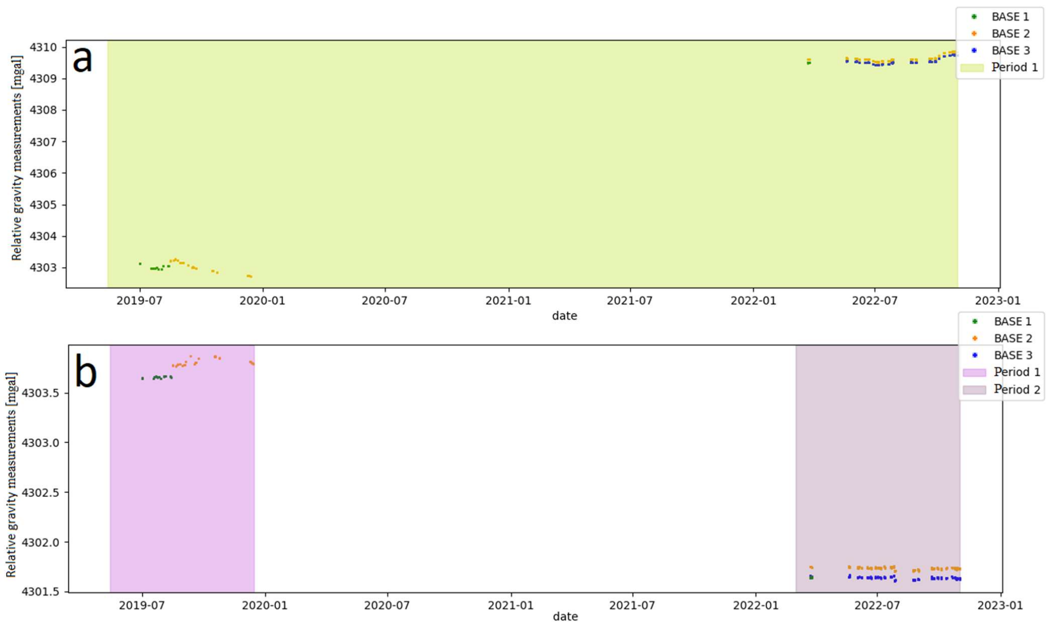

Figure B4: Result of intra-period drift correction after determining a one-period (a) and two-periods (b) drift function.

Where k is the number of parameters (and therefore periods) to be included in the model, n is the number of observations and L is the objective function, which in this case is a 10 µgal dispersion of the relative gravimeter readings at the three base

https://doi.org/10.5194/egusphere-2026-3978
Preprint. Discussion started: 24 September 2026

stations within the periods after drift correction. The result of these two criteria is shown in Fig. B5a and shows that the optimal number of periods to include in this drift correction step is 5. This also highlight the significant gain in accuracy between the drift function calculated over the whole campaign (Fig. B4a) and two functions calculated within each survey (Fig. B4b). The upper and lower limits of the periods used in these tests include only precise moments that separate important phases of the acquisition, such as the acquisition of different lines. Based on this observation, the MoreGeo 2019-2022 campaign was therefore divided into 5 periods. For each of these periods, an intra-period drift correction was calculated according to the principle presented above. The result of this intra-period drift correction is shown in Fig. B5b.

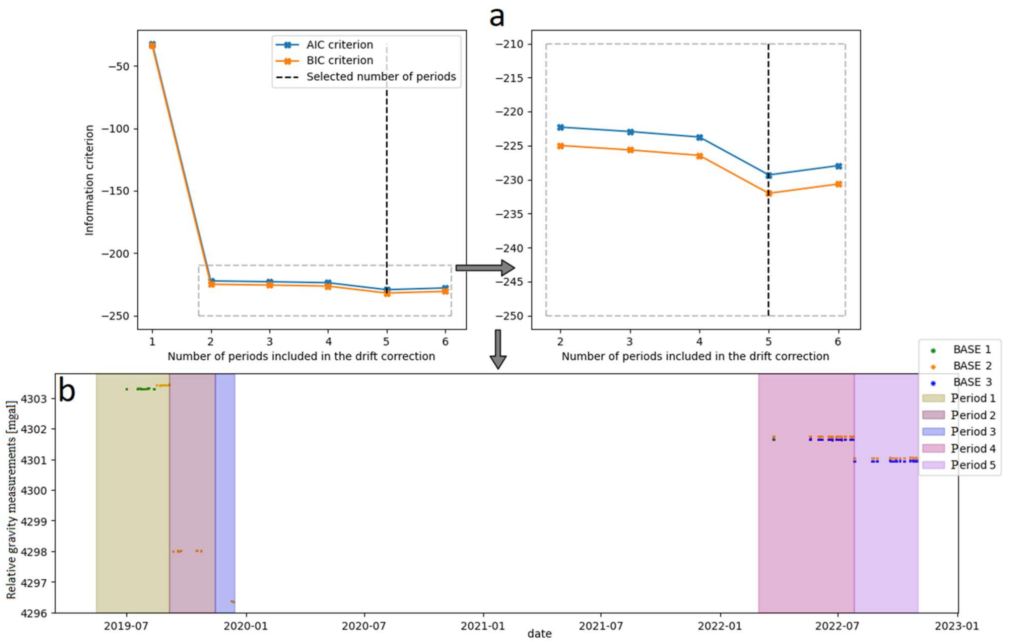

Figure B5: Selection of the number of periods according to the AIC and BIC criteria (a). Associated result of the intra-period drift correction on the three base stations (b).

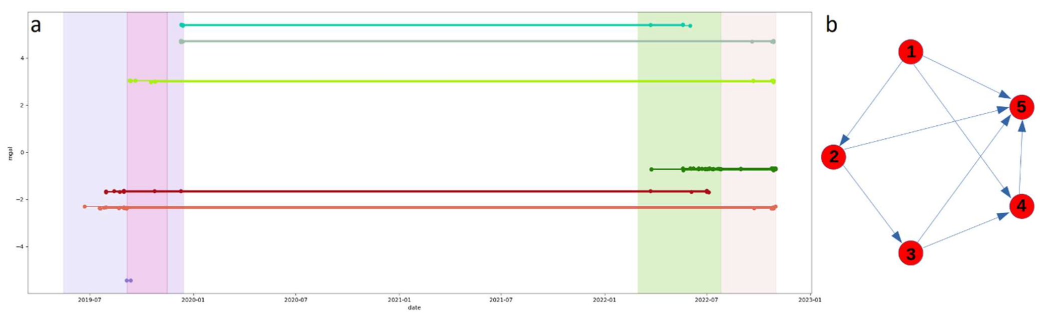

Figure B6: Closing loops between different periods that illustrate the inter-period offset relations after intra-period drift correction and filtering (a). Graph of inter-period offset relations (b).

Following this, the instrumental drift, corrected for each period from its start date, needs to be correct over the whole campaign. Called the inter-period correction, this second phase used the readings taken at the same station between different periods. A first simple approach would be to determine the offset to be applied between periods based on the average measurements obtained per period on one or more base stations. However, relying solely on records made at base stations is probably not the most effective way of repositioning the different periods knowing also that there is no single base station

https://doi.org/10.5194/egusphere-2026-3978
Preprint. Discussion started: 24 September 2026

used throughout the MoreGeo 2019-2022 campaign. Finally, there is the question of the choice of the reference period on which the whole campaign will have to base and on which the offset relation will depend.

In this sense, all the closing loops that connect the same station in two different periods have been selected. They are used to introduce the offset relations necessary to reposition the periods. Most of the inter-period offset relations are almost unambiguous, as the different relations linking these periods determine very similar offset values. Nevertheless, a few offset relations required filtering due to excessive dispersion. The Fig. B6a and Fig. B6b show respectively the offset relations filtered for period repositioning and the graph of the relations between periods in the MoreGeo case.

After filtering, the various offset relations form an overdetermined system of the form:

$$\begin{bmatrix} d_{\{15\}} \\ d_{\{15\}} \\ d_{\{15\}} \\ d_{\{23\}} \\ \dots \\ d_{\{45\}} \end{bmatrix} = \begin{bmatrix} \tilde{r}_{\{5_1\}} - \tilde{r}_{\{1_1\}} \\ \tilde{r}_{\{5_2\}} - \tilde{r}_{\{1_2\}} \\ \tilde{r}_{\{5_3\}} - \tilde{r}_{\{1_3\}} \\ \tilde{r}_{\{3_1\}} - \tilde{r}_{\{2_1\}} \\ \dots \\ \tilde{r}_{\{5_x\}} - \tilde{r}_{\{4_x\}} \end{bmatrix} \qquad (B9)$$

Where $\tilde{r}_{i_x}$ are the average relative gravimeter readings of the station x made in period i and d_{ij} are the unknown offsets between the two periods i and j for the same pair of x acquisitions. In addition to these equations, we also need to include closing relations, i.e. equations that loop over the same period and use more than two different offsets. In the case of MoreGeo, four independent closing relations have been determined using a modified Depth-First Search algorithm (Tarjan, 1972) with backtracking for closed cycles. The overdetermined system formed with all these equations has been solved using the Moore-Penrose inverse matrix method. This determines the best solutions in the sense of least squares (Barata, 2012) for all the offsets to be applied between linked periods in Fig. B6b.

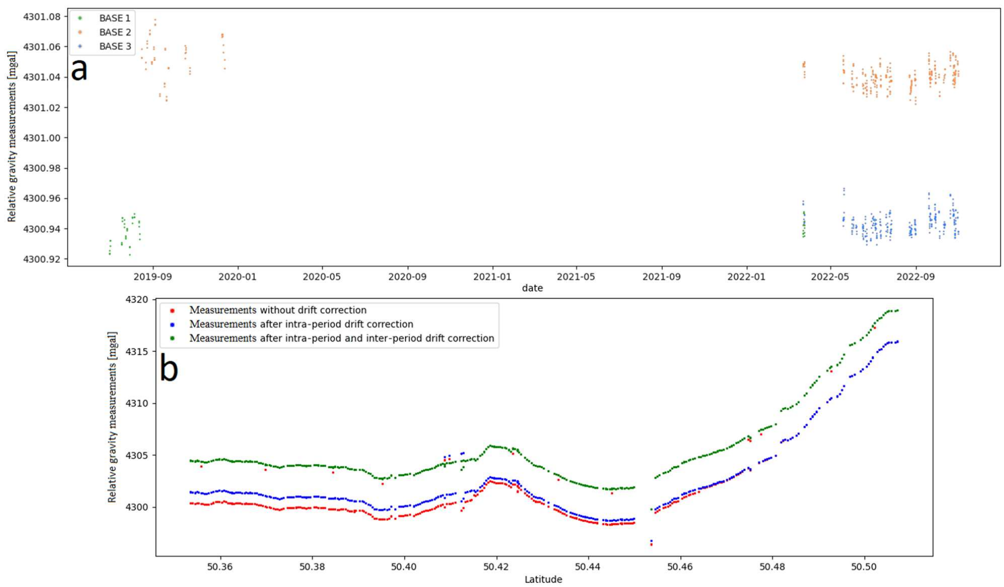

Figure B7: Relative gravimeter readings on the three base stations of the MoreGeo 2019-2022 campaign, after repositioning the periods to the fifth reference period (after intra-period and inter-period drift correction) (a). Relative effect of each phase of the drift correction on the relative gravimeter readings, Profile 2, S – N (b).

Concerning the reference period to which all the others can be repositioned on, the fifth seems to be the optimal choice since in the case of MoreGeo, all the others can be repositioned directly using solutions of Eq. B9. However, this ideal case does not occur systematically, and an iterative algorithm (based on Eq. B10) has been developed to deduce all other offsets between periods based on solutions of Eq. B9.

https://doi.org/10.5194/egusphere-2026-3978
Preprint. Discussion started: 24 September 2026

$$d_{ij} = \frac{1}{n}\sum_{k}^{n}\left(d_{ik} + d_{kj}\right) \text{ with } k \subset [1\text{:nbr of periods}]/(i,j) \tag{B10}$$

As the previous system of equations has been solved in the sense of least squares, the offset solutions depend on the period chosen and have a slight influence on the repositioning result. In the end, the reference period chosen is the one that includes the corrected readings at the three bases of the campaign with the least dispersion. In the case of MoreGeo, this was the fifth, which includes the resampling period at the end of October 2022. The dispersions, symbolised by the standard deviation of the corrected relative gravimeter reading at each of the three bases during the MoreGeo 2019-2022 campaign, are 9.6, 6.8 and 7.9 µgal, which is below the target accuracy of 10 µgal (Fig. B7a). The combined effect of inter- and intra-periodic corrections can also be seen in the relative gravimeter readings for profile 2 shown in the Fig. B7b.

Appendix C – Influence of the elevation and the grid extent in the local topographic correction

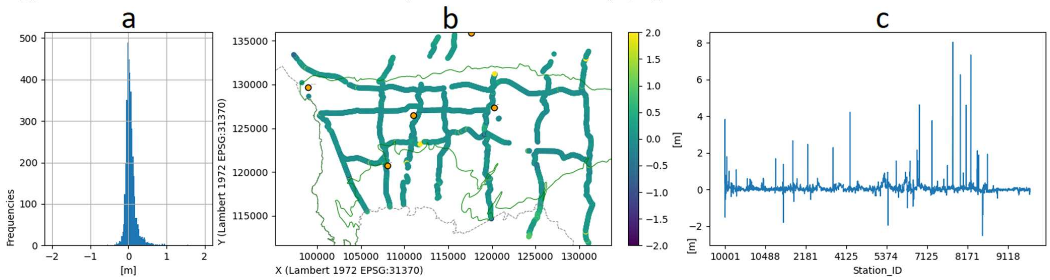

Figure C1: Histogram (a), regional map of spatial distribution (b) and temporal distribution (c) of EVRF2000 elevation differences at stations derived from the topographic survey and from the 1-meter-resolution DTM used for $\mathbf{A_{loc.\,T}}$.

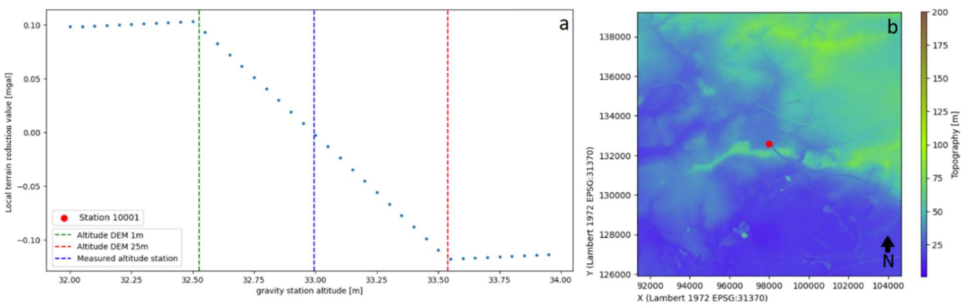

Figure C2: Influence of the elevation considered in the calculation of the local topographic correction at station 10001 and the transfer of the measured elevation (in blue) and the elevations of the first (in red) and second (in green) elevation grids (a). Location of gravimetric station 10001 (near the Bernissart town in Belgium) on the DTM at 1m resolution (b).

The height to consider when calculating the gravimetric influence of the prisms for the gravimetric station has been determined. This height must be consistent across stations for $\mathbf{A_{Reg.\,T}}$ and $\mathbf{A_{Loc.\,T}}$ and can be either the height referenced by one of the two grids at the station positions, or the height taken from the MoreGeo topographic survey. Intuitively, the latter seemed like the better option whereas the height of the 25 m resolution DTM appeared to be the worst. However, there are inevitable small differences between the surveyed heights and those of the 1m² resolution DTM (cf. Fig. C1 for illustrations about elevation differences). On Fig. C2, the case of station 10001 (near the Bernissart town in Belgium) was chosen to illustrate the impact of elevation selection in modelling. The elevation of this station taken from topographic survey in 2022 was 33 m (blue line), whereas the 1-meter and 25-meter resolution DTM indicate respectively an elevation of 32.52 m (green line) and 33.53 m (red line). In this figure, the cyan color dots represent the local topographic correction performed in an area extending 2 km, considering different observation elevations. It demonstrates that the choice of station height significantly alters the result. In this particular case, using the measured elevation gives a result close to zero, a consequence linked to the central position of the measured elevation within the prism formed by the two DTMs. On the basis of these observations, the 1m-resolution DTM elevation appears to be the elevation to be used in the two topographic corrections.

https://doi.org/10.5194/egusphere-2026-3978
Preprint. Discussion started: 24 September 2026

Regarding the grid size, the extent of the 1-meter resolution grid could possibly be reduced to improve computation time. Station 10001 was selected to model $\mathbf{A_{Loc.\,T}}$ based on the selected extent. Figure C3 shows that the accuracy targeted by the correction is quickly achieved with a grid extended to a few hundred metres. In particular, for a grid extended to 600 m around the station, the difference between the result obtained and that of the 6.65 km grid is less than 0.1 µgal, the accuracy of Scintrex CG6. In this work, an extension of 2 km around each station was chosen.

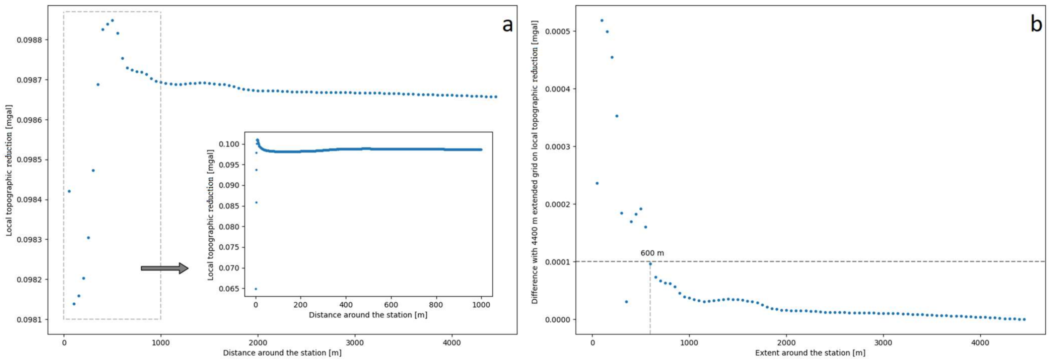

Figure C3: Result of the local topographic correction as a function of the extent of the grid used in the prism modelling for station 10001 (near the Bernissart town in Belgium) (a). Difference between the result of the local topographic correction obtained with a grid of increasing extent and a grid extended to 6.65 km around station 10001 (b).

Appendix D - Large-format version of Sect 3. figures

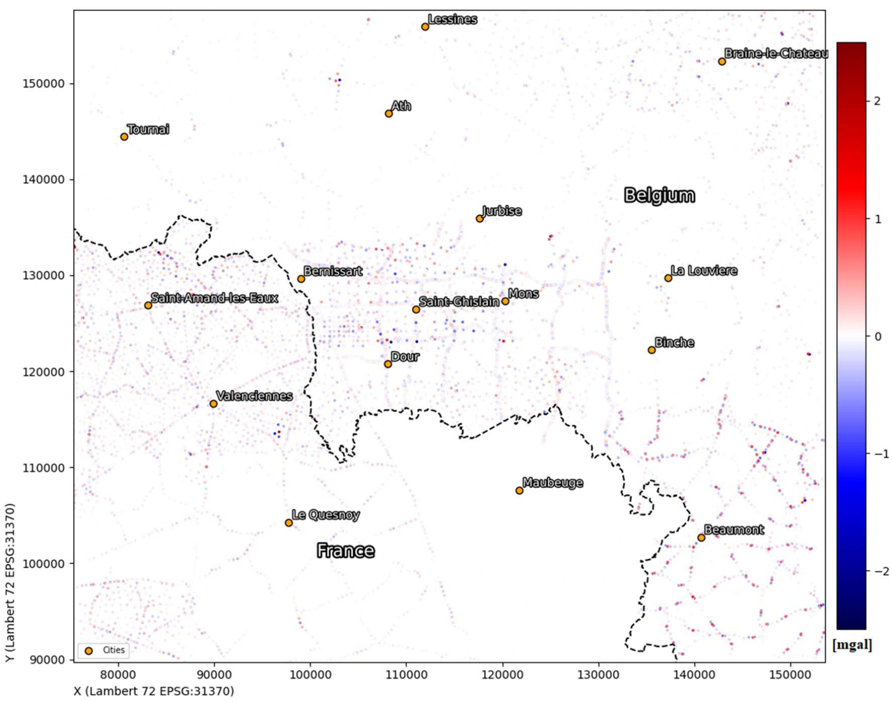

Figure D1. Comparison between the observed and simulated refined Bouguer anomaly data by the block-averaged equivalent sources method (source depth: 1250 m; damping: 0.5). Identification of systematic errors between observed and simulated data for the Dinant Basin campaign (1962) and of outliers in the Extension 1948 (1972) and Mons (1960) campaigns

https://doi.org/10.5194/egusphere-2026-3978
Preprint. Discussion started: 24 September 2026

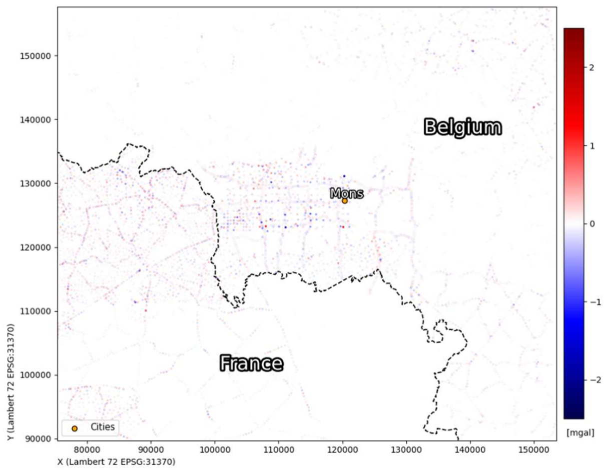

Figure D2. Comparison between the observed and the simulated refined Bouguer anomaly data by the block-averaged equivalent sources method after shifting the Dinant Basin (1962) data and eliminating outlier stations from extension 1948 (1972) and Mons (1960) campaigns (source depth: 1250 m; damping: 0.1).

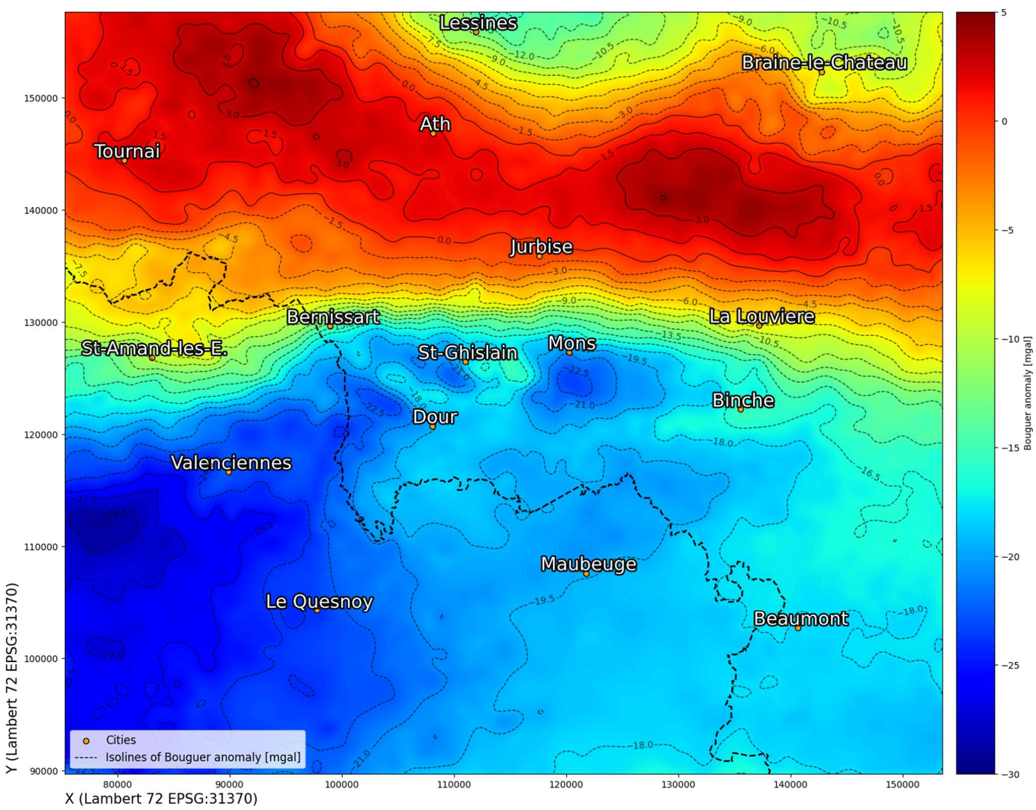

Figure D3: The updated refined Bouguer anomaly map and isovalue curves gridded with 200-metre resolution and predicted by the block-averaged equivalent sources method (reduction density of 2.67 g cm⁻³) in the French-Belgian Hainaut region.

https://doi.org/10.5194/egusphere-2026-3978
Preprint. Discussion started: 24 September 2026

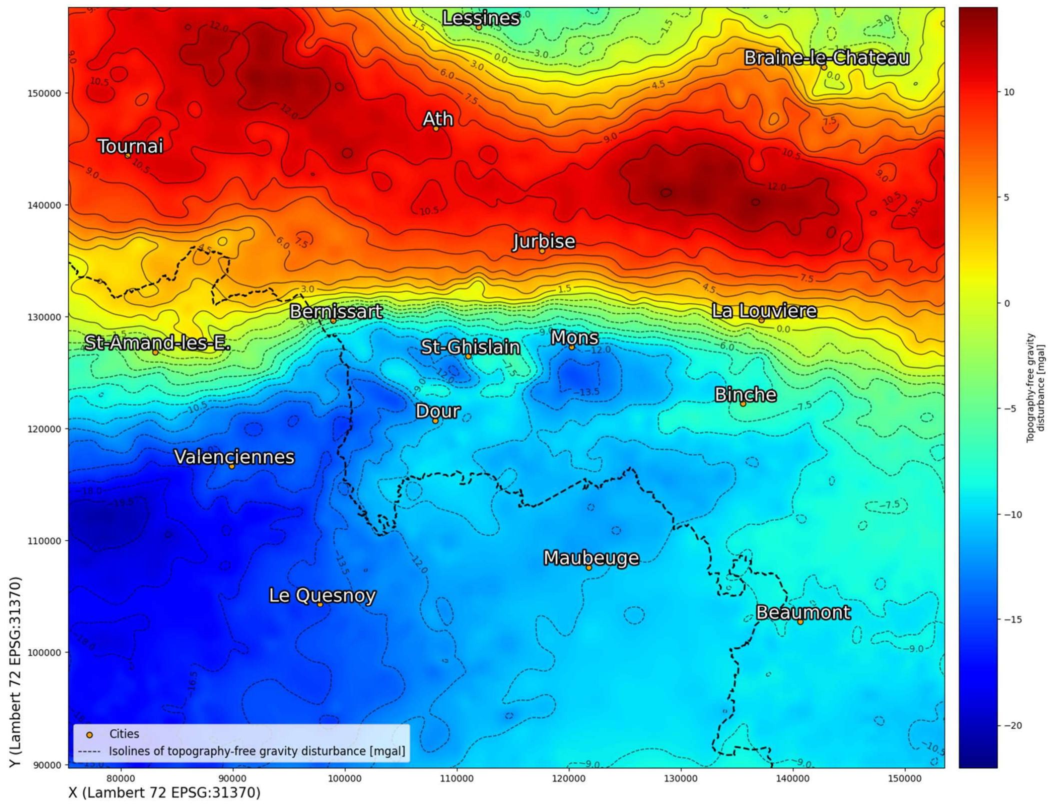

Figure D4: The topography-free gravity disturbance map and isovalue curves gridded with 200-metre resolution and predicted by the block-averaged equivalent sources method (reduction density of 2.67 g cm⁻³) in the French-Belgian Hainaut region.

References

Akaike, H.: A new look at the statistical model identification, IEEE T. Automat. Cont., 19(6), 716-723, doi: 10.1109/TAC.1974.1100705, 1974.

Barata, J. C. A., Hussein, M. S: The Moore–Penrose Pseudoinverse: A Tutorial Review of the Theory, Braz. J. Phys. 42, 146–165, https://doi.org/10.1007/s13538-011-0052-z, 2012.

Battaille Frères Society: Rapport sur une étude gravimétrique effectuée sur le polygone 5 du Borinage, Internal Report, Archives Geol. Surv. Belgium, 34, 1967.

Battaille Frères Society: Rapport sur une étude gravimétrique effectuée sur le polygone 3 et 8 du Borinage entre 1968 et 1969, Internal Report, Archives Geol. Surv. Belgium, 1 pl, 1969.

Belanger, I., Delaby, S., Delcambre, B., Ghysel, P., Hennebert, M., Laloux, M., Marion, J., Mottequin, B. and Pingot, J.: Redéfinition des unités structurales du front varisque utilisées dans le cadre de la nouvelle Carte géologique de Wallonie (Belgique), Geol. Belg., 15, 169-175, 2012.

BRGM : Banque Gravimétrique de France, Base de données, Data Open Access with WMS service : http://geoservices.brgm.fr/geologie, data download the 10 December 2023.

Bullard, E. C.: Gravity measurements in East Africa, Philos. T. Roy. Soc. A., 235, 445–534, 1936.

https://doi.org/10.5194/egusphere-2026-3978
Preprint. Discussion started: 24 September 2026

Campeol, Q.: Étude prospective des signatures diagraphiques du réservoir géothermique des calcaires carbonifères du Hainaut et de sa couverture Valorisation des diagraphies réalisées dans le sondage de Saint-Ghislain, Master's Thesis, UMONS - Faculty of Engineering, 165, 2021.

Campeol, Q., Dupont, N., Nanfo Djoufack, I. P., Christiaens, L., Martin, F., & Kaufmann, O.: new detailed Bouguer anomaly for the exploration of the deep geothermal reservoir in SW-Belgium. EGU General Assembly 2024, Vienna, Austria. doi:10.5194/egusphere-egu24-19287, 17 April 2024.

Campeol, Q., Dupont, N., & Kaufmann, O.: Processing of a new detailed Bouguer anomaly map in the Mons area, SW-Belgium, looking for deep-seated anomalies. Geologica Belgica Luxemburga Congress 2024, Liège, Belgium, 12 September 2024.

Campeol, Q., Kaufmann, O., Van Noten, K. and Lecocq, T.: Updating the National Gravity Database of Belgium in the French-Belgian Hainaut. BeNeLux Geography Days 2026, Leuven, Belgium. 08 April 2026.

Chantraine, J., Autran, A. and Cavelier, C.: Carte Géologique de la France au 1/1.000.000 : France, BRGM, 1996.

Cornet, J. and Stevens, C.: Relief du socle paléozoïque de la vallée de la Haine, Archives Geol. Surv. Belgium. 15 pl., 1921-1923.

Dampney, C. N. G.: The equivalent source technique. Geophysics, 34(1), 39–53, doi:10.1190/1.1439996, 1969.

Debacker, T. N., Sintubin, M. and Verniers, J.: Large-scale slumping deduced from structural and sedimentary features in the Lower Palaeozoic Anglo-Brabant fold belt, Belgium. J. Geol. Soc. London, 158, 341–352 pp. https://doi.org/10.1144/jgs.158.2.341, 2001.

Debacker, T. N., Herbosch, A., Verniers, J. and Sintubin, M.: Faults in the Asquempont area, southern Brabant Massif, Belgium. Neth. J. Geosci., 83, 49–65. https://doi.org/10.1017/S0016774600020461, 2004.

Delmer, A.: Le Bassin du Hainaut et le sondage de Saint-Ghislain, Prof. Pap. Geol. Surv. Belgium, 143, 24, 1977.

Delmer, A. and Van Wichelen, P.: Répertoire des puits naturels connus en terrain houiller du Hainaut, Professional Paper of Geological Survey of Belgium, 172, 79, 1980.

Dupont, N.: Analyse de la structure du socle paléozoïque hainuyer. Implications sur les caractéristiques des réservoirs profonds, PhD Thesis, UMONS - Faculty of Engineering – Geology and Applied Geology, Belgium, 374, 2021.

Dupont, N., Everaerts, M., Kaufmann, O., Campeol, Q., Nanfo djoufack, I. P. and Martin, F.: FEDER 2014-2020 – fiche MORE-GEO Délivrable n°2. Rapport de synthèse relatif à la modélisation gravimétrique sur le territoire du Cœur du Hainaut, Internal Report, 61, https://hdl.handle.net/20.500.12907/48043, 2023.

Ecker, E. and Mittermayer, E.: Gravity corrections for the influence of the atmosphere, Bull. Theor. Appl. Geophys, 11, 70-80, 1969.

Everaerts, M. and De Vos, W.: Gravity acquisition in Belgium and the resulting Bouguer anomaly map. Memoirs Geol. Surv. Belgium, 58, 55, 2012.

Everaerts, M. and Hennebert, M.: Interprétation géologique des données gravimétriques de la zone frontalière franco-belge, entre Bailleul et Beaumont. Ann. Soc. Géol. Nord, 6(2), 55-63 pp, 1998.

Francis, O.: Performance assessment of the relative gravimeter Scintrex CG-6. J. Geodesy, 95(10), 116, https://doi.org/10.1007/s00190-021-01572-y, 2021.

Ghiste, S. and Albert, B.: Carte géotechnique 45.7. 1. à 4 Mons (Secteur Mons-Jemappes-Cuesmes) au 1/10.000ème. Planche III b : Données générales de surface (comparaison avec la situation au XIXe siècle), 1pl, 1980.

Hammer, S.: Terrain Correction for Gravimetric Stations, Geophysics, 4, 184-194, 1939.

Fatiando a Terra Project, Castro, Y. M., Esteban, F. D., Li, L., Oliveira Jr, V. C., Pesce, A., Shea, N., Soler, S. R., Souza-Junior, G. F., Tankersley, M., Uieda, L., & Uppal, I.: Harmonica v0.7.0: Forward modeling, inversion, and processing

https://doi.org/10.5194/egusphere-2026-3978
Preprint. Discussion started: 24 September 2026

gravity and magnetic data (0.7.0). Zenodo. https://doi.org/10.5281/zenodo.13308312, 2024.

Fatiando a Terra Project, Bucha, B., Dinneen, C., Gomez, M., Li, L., Pesce, A., Soler, S. R., Uieda, L., & Wieczorek, M.: Boule v0.6.0: Reference ellipsoids for geodesy and geophysics (v0.6.0). Zenodo. https://doi.org/10.5281/zenodo.19333956, 2026.

Hartmann, T. and Wenzel, H.-G.: The HW95 tidal potential catalogue, Geophys. Res. Lett., 22, 24, 0094-8276, https://doi.org/10.1029/95GL03324, 1995

Hayford, J. F. and Bowie, W.: Geodesy: the effect of topography and isostatic compensation upon the intensity of gravity, Professional Paper of Coast and Geodetic Survey, 12, 1912.

Heck, B. and Seitz, K.: A comparison of the tesseroid, prism and point-mass approaches for mass reductions in gravity field modelling, J. Geodesy 81, 121–136, https://doi.org/10.1007/s00190-006-0094-0, 2007.

Heiskanen, W. A. and Moritz, H.: Physical Geodesy, 364, 1967.

Hofmann-Wellenhof, B. and Moritz, H.: Physical Geodesy. (2nd edition ed.), https://doi.org/10.1007/978-3-211-33545-1, 2006.

Hennebert, M.: Rôle possible des structures profondes du Massif cambro-silurien du Brabant dans l'évolution des bassins sédimentaires post-calédoniens (Belgique et Nord de la France), Ann. Soc. Géol. Belg., 116, 147–162, 1993.

Herbosch, A. and Debacker, T. N.: A new geological map of the outcrop areas of the Brabant Massif (Belgium), Geol. Belg., 21, 1-2, 41-58, https://doi.org/10.20341/gb.2018.003, 2018.

Hinze, W. J.: Bouguer reduction density, why 2.67?, Geophysics, 68, 1559–1560, 2003.

Kaufmann, O., Dupont, N., Campeol, Q., Martin, T., Thiebaut, E., and Goderniaux, P. Géothermie Profonde en Cœur de Hainaut (Belgique) – Contexte, réalisations et perspectives. Ann. Soc. Géol. Nord, 32, 0767-7367, https://doi.org/10.54563/asgn.2624, 2025.

LaFehr, T. R.: An exact solution for the gravity curvature (Bullard B) correction, Geophysics, 56, 8, 1179-1184, doi: https://doi.org/10.1190/1.1443138, 1991.

Lakshmanan, J.: The generalized gravity anomaly: Endoscopic microgravity. Geophysics, 56(5), 712-723. doi:10.1190/1.1443090, 1991.

Laurent, A.: Modélisation géologique 3D du bassin houiller du Nord-Pas-de-Calais et de son substratum dévonien-carbonifère inférieur : vers une meilleure définition des réservoirs géothermiques profonds, PhD Thesis, Lille, France : Université des Sciences et Technologies de Lille, 314, 2021.

Leclerc, M.: Levé gravimétrique du Bassin de Mons, essai d'interprétation, Master Thesis, Faculty of Engineering of Mons, 56, 1960.

Legrand, R.: Le Massif du Brabant. Mémoires pour servir à l'Explication des cartes Géologiques et Minières de la Belgique, 9, 148, 1968.

Leroy, G.: Analyse de l'évolution du niveau du sol à la limite d'exploitation minière du sud de Mons. Haute Ecole Léonard de Vinci, Master Thesis, 79, 2014.

Li, X. and Götze, H. J.: Tutorial: Ellipsoid, geoid, gravity, geodesy, and geophysics, Geophysics, 66(6), p. 1660-1668, doi:10.1190/1.1487109, 2001.

Licour, L.: Relations entre la géologie profonde et le comportement hydrogéologique du réservoir géothermique de Hainaut (Belgique) - Caractérisation de l'aquifère dans la région de Saint-Ghislain, PhD Thesis, University of Mons, 372, 2012.

Longman, I. M.: Formulas for computing the tidal accelerations due to the moon and the sun, J. Geophys. Res., 64, 12, 2351–2355, https://doi.org/10.1029/JZ064i012p02351, 1959.

Makhloof, A. A. The use of topographic isostatic mass information in geodetic applications, Institut für Geodäsie und Geoinformation der Universität Bonn., 156, 2008.

Mansy, J.-L., Everaerts, M. and De Vos, W.: Structural analysis of the adjacent Acadian and Variscan fold belts in Belgium and northern France from geophysical and geological evidence, Tectonophysics, 309, 99–116, https://doi.org/10.1016/S0040-1951(99)00134-1, 1999.

Martelet, G., Debéglia, N. and Truffet, C.: Homogénéisation et validation des corrections de terrain gravimétriques jusqu'à la distance de 167 km sur l'ensemble de la France, C. R. Geosci., Vo. 334(7), 449-454 pp. ISSN 1631-0713, https://doi.org/10.1016/S1631-0713(02)01779-0, 2002.

Martelet, G. and Deparis, J.: Banques gravimétrique et de données aéroportées de la France : travaux réalisés en 2010, tâches à réaliser en 2011. BRGM/RP-591 98-FR, 56 pp, 2010.

Minguely, B., Mansy, J.-L., Hanot, F., Everaerts, M., Lacquement, F. and Averbuch, O.: Synthèse des données de sondage et des données gravimétiques depuis l'Avesnois jusqu'au méridien de Lens: résultats préliminaires. Géologie de la France, 1-2, 93-98, 2006.

Minguely, B.: Caractérisation géométrique 3-D de la couverture sédimentaire méso-cénozoïque et du substratum varisque dans le Nord de la France : apports des données de sondages et des données géophysiques, PhD Thesis, Lille University of Science and Technology, 231, 2007.

Molodensky, M. S., Yeremeev, V. F. and Yurkina, M. I.: Methods for Study of the External Gravitational Field and Figure of the Earth. TRUDY Ts NIIGAiK, 131. Geodezizdat, Moscow (English translat.: Israel Program for Scientific Translation, Jerusalem 1962), 1960.

Moritz, H.: Geodetic reference system 1980, B. Geod., 54, 395–405, https://doi.org/10.1007/BF02521480, 1980.

Nagy, D.: The gravitational attraction of a right rectangular prism, Geophysics, 31, 2, 362-371, 1966.

Nagy, D.: The prism method for terrain corrections using digital computers, Pure Appl. Geophys., 63, 31-39, https://doi.org/10.1007/BF00875156, 1966.

Nagy, D., Papp, G. and Benedek, J.: The gravitational potential and its derivatives for the prism, J. Geodesy, 74, 552, https://doi.org/10.1007/s001900000116, 2000.

Nagy, D., Papp, G. and Benedek, J.: Corrections to "The gravitational potential and its derivatives for the prism", J. Geodesy., 76, 8, 475-475, https://doi.org/10.1007/s00190-002-0264-7, 2002.

Nowell, D. Gravity terrain corrections - an overview, J. Appl. Geophy., 42, 117-134, https://doi.org/10.1016/S0926-9851(99)00028-2, 1999.

Oliveira Jr, V. C., Uieda, L., Hallam, K. A. and Barbosa, V. C. F.: Should geophysicists use the gravity disturbance or the anomaly. Geol. Phys., 2018.

Petitclerc, E. and Vanbrabant, Y.: Développement de la plate-forme Géothermique de la Wallonie. Rapport final. Rapport public. Direction Générale Opérationnelle de l'Aménagement du territoire, du Logement, du Patrimoine et de l'Energie (DGO4), Energy Department, Royal Belgian Institute of Natural Sciences, Geol. Surv. Belgium, 228, 2011.

Piguet, J.-P.: Evaluation des effets de surface dus aux voies et galeries minières anciennes du houiller, Internal INERIS Report, ref. SSE-JPP/DK-97-26EE54/RN01., 1997.

Phillips, J. D.: 11.12 - Tools and Techniques: Gravitational Method, Treatise on Geophysics (Second Edition), 393-418, ISBN 978-0-444-53802-4, https://doi.org/10.1016/B978-0-444-53802-4.00197-4, 2015.

Rubio, F. M., Rey-Moral, C., Ayala, C., García, A. G., Durán, A. G., Delgado, J. M. L. and Mediato, J. F.: D2. 2 GRAVIMETRIC SURVEY, LOPÍN STRUCTURE, ONSHORE EBRO BASIN, SPAIN. *Changes*, *1*, 2, 2022.

Schüler, T.: Conducting and Processing Relative Gravity Surveys. *Institute of Geodesy and Navigation. University FAF*

https://doi.org/10.5194/egusphere-2026-3978
Preprint. Discussion started: 24 September 2026

Munich, Germany, 2000.

Slobbe, C., Klees, R., Farahani, H. H., Huisman, L., Alberts, B., Voet, P. and Doncker, F. D.: The Belgian hybrid quasi-geoid. HBG18, 1, 2018.

Snow, A. D., Cochran, M., Miara, I., Hoese, D., Van den Bossche, J., Mayo, C., Lucas, G., Cochrane, P., de Kloe, J., Karney, C., Jimenez Shaw, J., Quoc Anh, T., Filipe, Ouzounoudis, G., Couwenberg, B., Lostis, G., Dearing, J., Jurd, B., Gohlke, C., Schneck, C., McDonald, D., Taves, M., Itkin, M., May, R., Stewart, A. J., de Bittencourt, H., Little, B., Hugonnet, R., and Rahul, P. S.: pyproj4/pyproj: 3.7.2rc1 (3.7.2rc1), Zenodo, https://doi.org/10.5281/zenodo.16817340, 2025

Soler, S. R. and Uieda, L.: Gradient-boosted equivalent sources, Geophys. J. Int., 227, 3, 1768-1783. https://doi.org/10.31223/X58G7C, 2021.

Stevens, C. and Marlière, R.: Révision de la carte du relief du socle paléozoïque du bassin de Mons, Ann. Soc. Géol. Belg., 57, B145-B175, 1944.

Talwani, M.: Errors in the total Bouguer reduction, Geophysics, 63, 1125-1130, https://doi.org/10.1190/1.1444412, 1998.

Tamura, Y.: A harmonic development of the tide-generating potential. *Bull. d'Inf. Marées Terr.*, *99*, 6813-6855, 1987.

Tarjan, R. E.: Depth-First Search and Linear Graph Algorithms, SIAM J. Comput., 1, 2, 146–160. https://doi.org/10.1137/0201010, 1972.

Vajda, P., Ellmann, A., Meurers, B., Vaníček, P., Novák, P. and Tenzer, R.: Global ellipsoid-referenced topographic, bathymetric and stripping corrections to gravity disturbance, Stud. Geophys. et Geod., 52, 19-34, 2008.

Van Camp, M., and Vauterin, P.: "Tsoft: graphical and interactive software for the analysis of time series and Earth tides." *Computers & Geosciences*, 31(5), 631-640, 2005.

Verbeurgt, J., Van Camp, M., Stal, C., Camelbeeck, T., De Sloover, L., Poppe, H., Declercq, P.-Y., Voet, P., Constales, D., Troch, P., De Maeyer, P. and De Wulf, A.: The gravity database for Belgium, Geosci. Data J., 6, 2, 116-125, Data Open Access: https://doi.org/10.24414/j0dx-9n36, 2019

Wit, E., Heuvel, E.v.d. and Romeijn, J.-W.: 'All models are wrong...': an introduction to model uncertainty, Stat. Neerl., 66, 217-236, https://doi.org/10.1111/j.1467-9574.2012.00530.x, 2012.